

**COMPUTATIONAL MODELING OF PROJECTION TWO-
PHOTON LITHOGRAPHY AND EVALUATION OF
PROCESS LIMITS**

A Dissertation
Presented to
The Academic Faculty

by

Rushil Pingali

In Partial Fulfillment
of the Requirements for the Degree
Master of Science in the
School of Mechanical Engineering

Georgia Institute of Technology
May 2023

COPYRIGHT © 2023 BY RUSHIL PINGALI

**COMPUTATIONAL MODELING OF PROJECTION TWO-
PHOTON LITHOGRAPHY AND EVALUATION OF PROCESS
LIMITS**

Approved by:

Dr. Sourabh Saha, Advisor
School of Mechanical Engineering
Georgia Institute of Technology

Dr. Amit Jariwala
School of Mechanical Engineering
Georgia Institute of Technology

Dr. Yan Wang
School of Mechanical Engineering
Georgia Institute of Technology

Date Approved: 4/28/2023

ACKNOWLEDGEMENTS

This work was supported by the National Science Foundation CAREER Grant 2045147 and in part through research cyberinfrastructure resources and services provided by the Partnership for an Advanced Computing Environment (PACE) at the Georgia Institute of Technology. I would like to thank my advisor, Dr. Sourabh Saha, for the opportunity to conduct research as an undergraduate and graduate student, and for providing continued support and guidance. I would also like to thank my committee members, Dr. Amit Jariwala and Dr. Yan Wang, for their feedback and advice.

TABLE OF CONTENTS

ACKNOWLEDGEMENTS	iii
LIST OF TABLES	v
LIST OF FIGURES	vi
LIST OF SYMBOLS AND ABBREVIATIONS	viii
SUMMARY	x
CHAPTER 1. Introduction	1
1.1 Two-Photon Lithography	1
1.1.1 Process Physics	1
1.1.2 Applications	3
1.2 Projection Two-Photon Lithography	4
1.3 Motivations for Computational Modeling of TPL	7
CHAPTER 2. Reaction-Diffusion Modelling	10
2.1 Chemical and Mathematical Foundation	10
2.2 Optical Inputs	14
2.3 Reaction-Diffusion Model Parameters	16
2.3.1 Calibration Scheme	17
2.3.2 Experimental Determination of DOC_{th}	18
2.4 Finite Element Modeling in COMSOL	20
2.4.1 2D Model	21
2.4.2 3D Model	28
CHAPTER 3. Neural Network Surrogate Modeling	33
3.1 Training Data Set Collection	34
3.2 Neural Network Design and Performance	38
CHAPTER 4. Experiments, Results, and Discussion	40
4.1 Investigation of Proximity Effects	40
4.2 Investigation of Resolution Limits of Nanowire Printing	43
4.3 Generation of Printability Maps	52
CHAPTER 5. Conclusion	55
APPENDIX A. High Performance Computing Tools	57
A.1 Batch Processing on HPC	58
A.2 Dynamic Programming for Multiple Exposure Studies	61
REFERENCES	62

LIST OF TABLES

Table 1: Parameters and Initial Conditions for Reaction-Diffusion Model	p. 16
Table 2: Neural Network Data Collection Parameters	p. 36
Table 3: Multiple Projection Experiment Parameters	p. 44
Table 4: Comparison of NN and FEA solve times	p. 54

LIST OF FIGURES

Figure 1: Projection TPL. (A) Digital masks are projected layer-by-layer to form printed structures. (B) A micromirror array is used to apply the digital mask. (C) Temporal focusing limits printing to the focal plane. Diagram reproduced from previously published work [31].	p. 5
Figure 2: Complex 3D microstructures fabricated through P-TPL [31].	p. 7
Figure 3: (A) DMD digital mask image (B) X-Z dosage distribution for $y = 0$ plane	p. 15
Figure 4: Presence or absence of printing for different exposure durations	p. 19
Figure 5: Raman spectrogram for exposed and unexposed sample	p. 20
Figure 6: 2D model geometry and mesh	p. 22
Figure 7: Mesh convergence for 2D model. Simulation of five 3 px lines with 1.2 ms exposure.	p. 22
Figure 8: Solver time step size over the course of a model solve	p. 23
Figure 9: Degree of conversion profile at different times	p. 25
Figure 10: DOC, $[R^*]$ and $[O_2]$ at the center of the center line	p. 26
Figure 11: A: DOC. B: $DOC > DOC_{th}$	p. 27
Figure 12: Predicted versus measured nanowire widths and heights for different beam powers [36]	p. 28
Figure 13: 3D model geometry and mesh	p. 29
Figure 14: Mesh convergence for 3D model. Simulation of log-pile structure depicted in Figure 15.	p. 29
Figure 15: 3D model results, printed region at different times	p. 30
Figure 16: Solve time vs. degrees of freedom for 2D and 3D models, 50 pulses.	p. 31
Figure 17: Degree of Conversion for simulation of 5 parallel lines after 10 pulse exposure, $y = 0$ plane (a) from 3D model (b) from 2D model	p. 32
Figure 18: Printing Outcomes: A) No Printing B) Printing C) Overprinting	p. 35

Figure 19: Neural Network Structure [43]	p. 38
Figure 20: Confusion Matrix for Neural Network Results [43]	p. 39
Figure 21: Temporal evolution of chemical species concentration at center of center line for a projection of 5 x 5 px lines (a) normal O ₂ (b) 5% of normal O ₂ ...	p. 41
Figure 22: O ₂ drop off from the center of the center point in lateral and axial directions, various times. (a) and (b) for normal [O ₂], (c) and (d) for 5% of normal [O ₂]	p. 42
Figure 23: Center line resolutions achievable by multiple projections vs. single projections	p. 46
Figure 24: Distribution of center line dimensions	p. 47
Figure 25: Center line DOC vs. width	p. 48
Figure 26: Center line DOC vs. height, constant 600nm width	p. 49
Figure 27: Width of rightmost and center lines	p. 50
Figure 28: Line width vs. total exposure time	p. 51
Figure 29: Printability Map, NN & FE datapoints, k_p (dm ³ /mol /s) - k_t (dm ³ /mol /s)	p. 52
Figure 30: Printability Map, NN & FE datapoints, k_p (dm ³ /mol /s) – k_q (dm ³ /mol /s)	p. 53
Figure 31: Batch Solving and Processing of FE P-TPL Simulations	p. 59
Figure 32: Dynamic Programming Workflow for Multiple Projection Sweep	p. 63

LIST OF SYMBOLS AND ABBREVIATIONS

Chemical Species

PI	photoinitiator
R*	primary radical
PETA	pentaerythritol triacrylate
O ₂	oxygen
P*	active polymer chain
R ^x	quenched primary radical
P ^x	dead polymer chain

Symbols

k_p	polymerization rate constant
k_q	radical quenching rate constant
k_t	termination rate constant
D_{R^*}	diffusivity of R*
D_{O_2}	diffusivity of O ₂
DOC_{th}	threshold degree of conversion
D_p	dosage per pulse
$\sigma^{(2)}$	two-photon cross section
h	Planck's constant
Φ	quantum yield
ν	frequency of light

A k_p exponential function shape
 B k_t exponential function shape

Abbreviations

TPL Two-photon lithography
P-TPL Projection two-photon lithography
DLW Direct-laser writing
3D Three dimensional
TPA Two-photon absorption
DOC Degree of conversion
DMD Digital micromirror device
NN Neural network
LHS Latin hypercube sampling
HPC High performance computing
ReLU Rectified linear unit
PACE Partnership for an Advanced Computing Environment
U.V. Ultraviolet

SUMMARY

Two-photon lithography (TPL) is a direct laser writing technique that is capable of printing cm-scale three-dimensional structures with submicron-scale features. Projection two-photon lithography (P-TPL) is a variant of TPL that is a thousand times faster than conventional point-by-point processing techniques. P-TPL achieves faster printing by enabling the projection and printing of entire layers at once. However, its practical utility is limited by the lack of accurate process models. P-TPL is challenging to computationally model because the timescales vary from femtoseconds to seconds and the length scales vary from tens of nanometers to hundreds of micrometers. In this work, the first physics-based computational models of the photopolymerization processes underlying P-TPL are developed. The resulting reaction-diffusion model is capable of accurately predicting feature sizes under various printing conditions. A surrogate machine learning model is trained on data generated from reaction-diffusion simulations and is shown to be capable of rapidly predicting printability across large parameter spaces. These simulation capabilities are used to characterize the performance and operating limits of P-TPL. Specifically, defects due to chemical proximity effects arising from oxygen diffusion are studied and methods of minimizing them are devised. Additionally, rate and resolution limits are characterized, and strategies to maximize both objectives by printing with combinations of multiple projections are evaluated. Through the use of the surrogate models, the broader P-TPL parameter space is explored and a map of printable regimes is generated. These simulation capabilities represent an important step towards achieving a truly scalable nanoscale additive manufacturing technology.

CHAPTER 1. INTRODUCTION

1.1 Two-Photon Lithography

Since the development of the femtosecond laser in the 1990s, two-photon lithography (TPL) has established itself as a gold-standard technique for the fabrication of complex nanoscale structures with resolutions below 100 nm [1-3]. Like other direct-laser writing (DLW) processes, TPL allows for precise and continuous deposition of printed material over digitally programmed paths [4]. Critically for many nanotechnology applications, structures fabricated by TPL can be truly three-dimensional (3D) and freestanding [1].

1.1.1 Process Physics

The optical process behind TPL is two-photon absorption (TPA), a phenomenon first theorized by Maria Göppert-Mayer in 1931 and demonstrated experimentally in 1961 [5]. Two-photon absorption refers to a molecule making an electronic transition to a higher energy level after absorbing two successive photons. In contrast to single-photon absorption, TPA is an inherently non-linear process with respect to light intensity. While this attribute allows for higher resolutions, it also requires femtosecond lasers to achieve the high intensities necessary for TPA [6]. The extremely short pulse durations of such lasers mean that high power can be achieved while delivering low amounts of total energy, thus preventing damage to the sample.

In two-photon lithography, the TPA process does not always take place in all components of the photoresist itself, but in compounds known as photoinitiators that are specifically designed to be sensitive to multiphoton absorption. This attribute is quantified

as the two-photon cross-section $\sigma^{(2)}$, which has units of $\text{cm}^4\text{s photon}^{-1}$ [7]. Some proportion of excited photoinitiator molecules form free radicals that drive the polymerization process; this proportion is known as the quantum yield or quantum efficiency [8]. Thus, the ideal photoinitiator has a high two-photon cross-section and also forms radicals with high quantum efficiency, allowing for efficient printing with minimal energy requirements.

The photoresist used in TPL is typically a monomer or oligomer mixture such as an acrylate or polyacrylate. The process chemistry of TPL involves the conversion of these monomers into insoluble polymer through free-radical propagation [6]. The percentage of monomer converted to polymer is referred to as the degree of polymerization or degree of conversion (DOC). The polymerization process itself follows a typical free-radical chain reaction scheme, with several different possible initiation, quenching, propagation, and termination reactions [9].

Notably, the rapid quenching of free radicals by dissolved oxygen or other inhibitors introduces a further non-linearity in the TPL process. At low light intensities, the concentration of free radicals is low enough that the reaction is suppressed through quenching before significant polymerization has had a chance to occur. Combined with the previously discussed optical non-linearity of two-photon absorption, this introduces a strong thresholding effect for TPL; at low laser powers or short exposures, only the center of the focal spot receives enough dosage to polymerize, while the surrounding regions are quenched [6]. Finally, a third non-linearity arises from the presence of a solubility threshold in the photoresist. At low degrees of conversion, the polymer is soluble and washed away during development. Only regions with a DOC above a threshold DOC remain after

development [10]. The combination of these non-linearities allows for the hallmark capability of TPL to print structures far smaller than the diffraction limit of its optical systems.

1.1.2 Applications

Consequently, TPL has carved out a niche in the fabrication of high-resolution polymer nanostructures. It has been recognized as one of the most versatile and precise choice for the fabrication of microneedle patches that can be used for non-invasive drug or vaccine delivery [11]. Researchers have used TPL to create miniaturized endoscopy tubes without the optical limitations of probes built using competing fabrication techniques, allowing for high-quality imaging of arteries and small organs [12]. Beyond medicine, another field that TPL has seen numerous successful applications in is the fabrication of micro-lenses and optics. Schmid et al. demonstrated the fabrication of achromatic and apochromatic lenses through the combination of refractive and diffractive surfaces [13], while Dietrich et al. printed beam-shaping elements for applications in integrated optics [14]. Other applications of TPL have been in micro-machines [15], anti-counterfeiting [15], high energy density physics [16], tissue engineering [17, 18] and many other fields [19-27]. Although TPL technology remains largely in the development phase, efforts to commercialize TPL have also made progress. Companies manufacturing high-performance TPL systems for research and industry customers include Nanoscribe GmbH, Microlight3D, and Femtika [28, 29].

1.2 Projection Two-Photon Lithography

Despite these successes, wider deployment of two-photon lithography has been limited by its slow rate of processing, caused by the serial nature of its point-by-point writing scheme. With processing rates ranging from $10 \mu\text{m s}^{-1}$ to 100mm s^{-1} [30], serial TPL is only suitable for the manufacture of small, bespoke structures. Printing at higher rates than this has generally involved a trade-off in resolution [31].

Hence, there is significant research interest in increasing the processing rate of TPL to make rapid mass-manufacture of nanoscale structures feasible. One promising technology pioneered in our research group is Projection Two Photon Lithography (P-TPL). In P-TPL, the traditional serial writing scheme is replaced by a layer-by-layer parallel projection scheme. This paradigm allows for throughput up to a 1000 times greater than that of serial TPL, with no loss of resolution or precision [31].

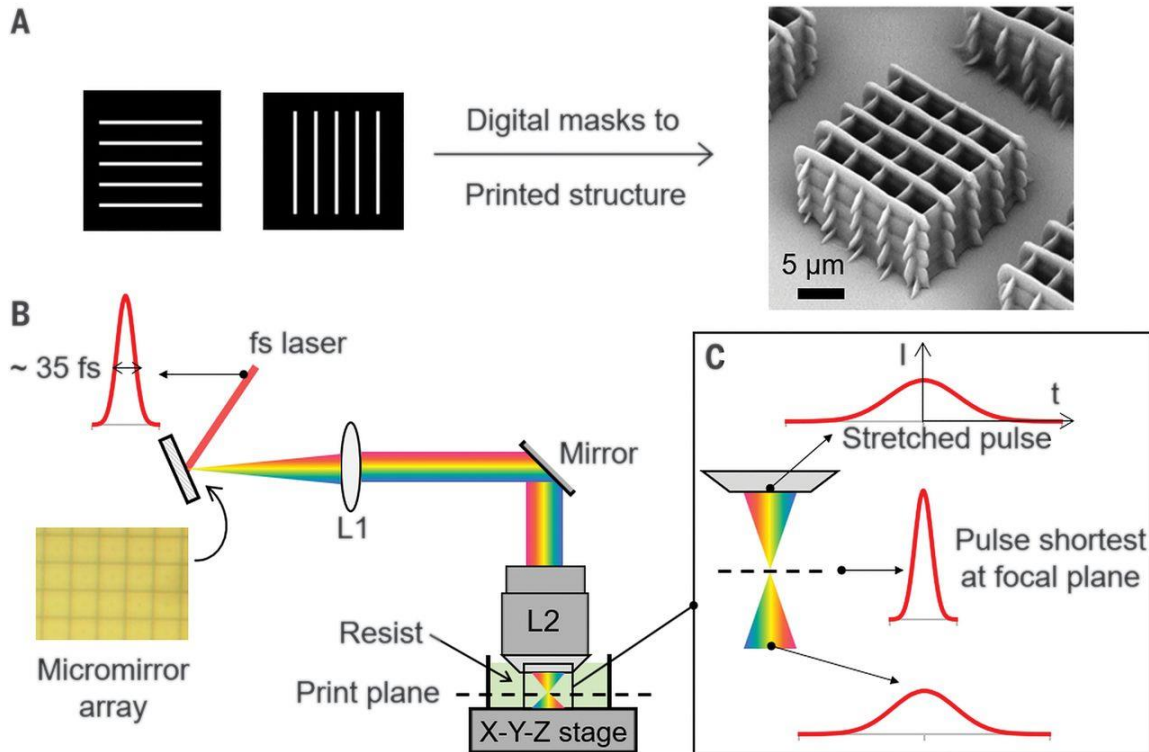


Figure 1: Projection TPL. (A) Digital masks are projected layer-by-layer to form printed structures. (B) A micromirror array is used to apply the digital mask. (C) Temporal focusing limits printing to the focal plane. Diagram reproduced from previously published work [31].

Figure 1 shows the P-TPL setup. A femtosecond laser is used; however, the laser is first directed off a digital micromirror device (DMD). The DMD allows for projection of an entire light sheet rather than a single point. Through its array of individually controllable mirrors, the DMD can be used as a digital mask, with only selected pixels being illuminated in the desired pattern for printing. Each such light sheet is the equivalent of over a million separate focal points and can be less than 1 μm thick [31]. P-TPL maintains depth resolution through the use of temporal focusing, illustrated in Figure 1C. In order to ensure that printing occurs only in the focal plane and not above or below it, an intensity gradient is generated by shortening the pulse duration as it travels through the photoresist such that the requisite light intensity is only achieved in the focal plane. In

contrast to a fixed mask, the DMD digital mask can be rapidly updated with the desired pattern for the next projection. After the stage is moved in the z -direction to locate the focal plane at the desired position, the next layer can immediately be printed, enabling massive parallelization that is completely independent to the percentage of each layer that is printed. The projection system also allows for the printing of complex patterns in the x - y plane (projected light sheet) without needing complex tool paths and stage movements [31]. Some such printed structures are shown in Figure 2. After printing, samples are exposed to U.V. light to increase their DOC and improve mechanical properties further [32].

Thus, through the use of simultaneous spatial and temporal focusing, P-TPL breaks the rate vs. resolution trade-off described previously, and is an important step towards scaling up TPL for widespread use.

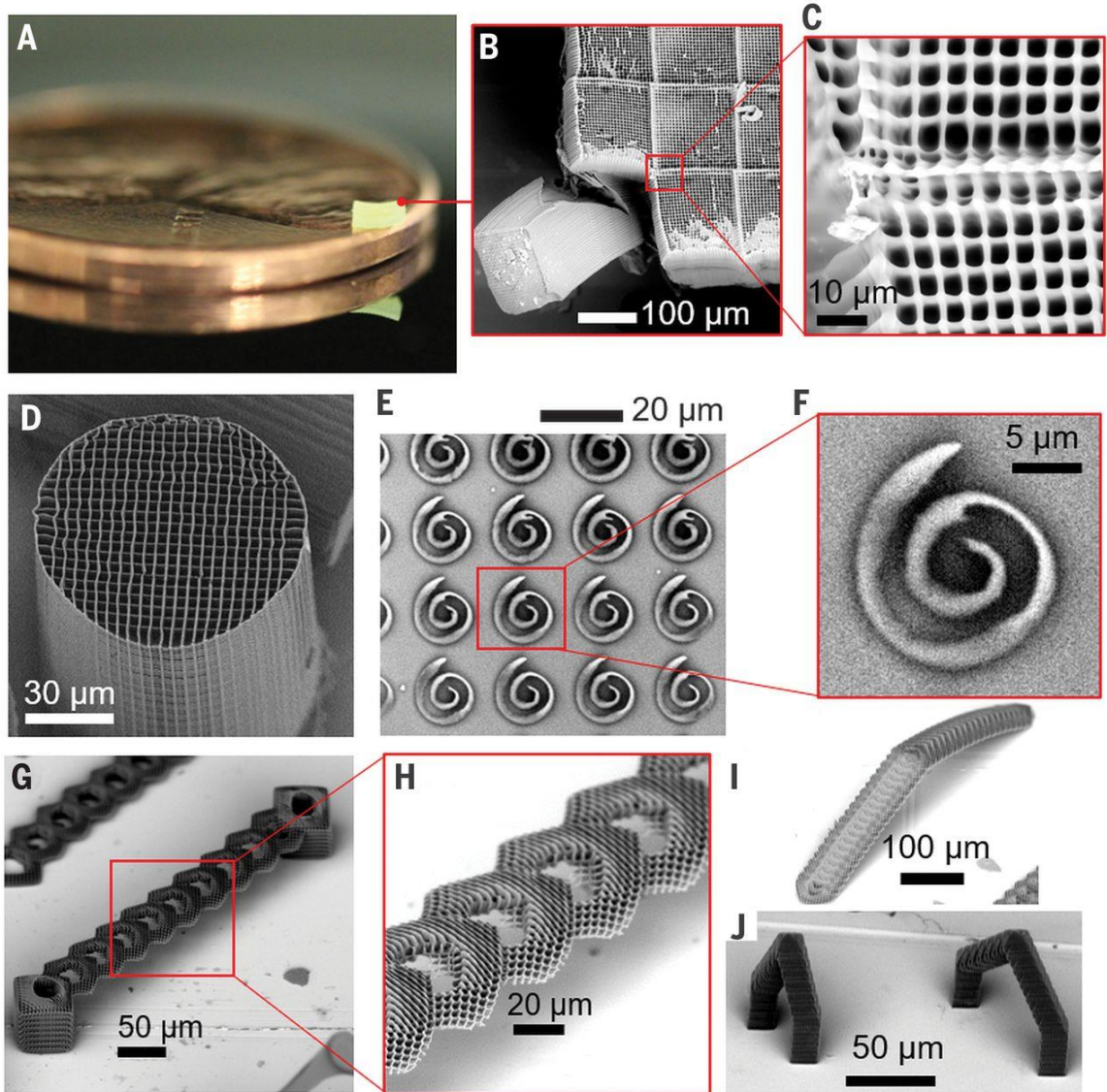


Figure 2: Complex 3D microstructures fabricated through P-TPL [31].

1.3 Motivations for Computational Modeling of TPL

Today, the development of robust simulation and modelling abilities is almost a prerequisite for an advanced manufacturing technology to achieve true scalability. A trial-and-error approach is impractical for anything more than the simplest design problems. A

robust computer model can predict manufacturing outcomes with satisfactory accuracy in a fraction of the time required to physically manufacture and characterize a part. A sufficiently quick-to-solve model can even be used for inverse design problems, where the desired outcome is specified and manufacturing conditions are reverse-engineered through computational optimization methods [33]. Both forward and inverse design capabilities are critical to bringing a technology out of the lab and to a broader market [34].

For this reason, there has been considerable interest in developing increasingly sophisticated models for TPL. Several research groups have taken different approaches to tackling this simulation problem, and have produced models of varying complexity, evaluation speed, and accuracy. For example, Hadibrata et. al applied an optimization procedure for the inverse design of a metalens that they then fabricated through TPP [33]. Uppal and Shiakolas modelled temperature effects and investigated their effects on voxel growth [34]. Mueller et. al utilized a numerical model in their investigation of TPL polymerization kinetics [35].

However, these models for serial TPL have important limitations. Models variously either do not consider the pulsed nature of radical generation in TPL, focus exclusively on optical modeling, do not treat diffusion, or do not consider a solubility threshold for actual feature size measurements [33-35]. Furthermore, the projection-based parallelization scheme of P-TPL alters the length and time scales of the TPL process, so serial models cannot simply be applied to predict P-TPL outcomes. While serial TPL exposes only a small area at a time, P-TPL exposes an entire layer of side lengths $>100\ \mu\text{m}$ at once. Conversely, pulsed exposure events in serial TPL occur only $\sim 10\ \text{ns}$ apart, while P-TPL exposures, although extremely fast, have gaps of $0.2\ \text{ms}$ or greater between them [36].

These differences must be taken into account for a computational model to accurately predict P-TPL printing.

Simulation work that provides fundamental insights into the physics of the TPL process has the potential to accelerate research in a field that has thus far been dominated by experiment-based empirical research work. In particular, characterizing and overcoming the resolution limits and proximity-effect-induced defects is central to understanding P-TPL process limits, as is mapping the parameter space to distinguish printable regimes. Robust simulation capabilities are a prerequisite to answering these questions that constitute the objective of this work.

Thus, the development of a computational model of the P-TPL process was chosen to be the focus of the research in this thesis, motivated by the compelling benefits of a robust simulation capability in furthering understanding and enabling scaling up of the technology. In the following chapters, this work will describe the development of a high-fidelity reaction-diffusion model of the P-TPL process as well as low-fidelity surrogate models for rapid evaluation. Using these models, an exploration of the parameter space and an evaluation of the resolution limits of the P-TPL process will be conducted.

CHAPTER 2. REACTION-DIFFUSION MODELLING

2.1 Chemical and Mathematical Foundation

The chemistry of two-photon lithography is centred on the free-radical chain reaction polymerization of multifunctional monomers and includes the typical steps for such reactions. Primary radicals are formed in the initiation step in the presence of light; they combine with monomer molecules to start polymer chains that grow through the addition of more monomers. This propagation step is also accompanied by chain transfer and cross-linking side reactions. The chain reaction ends when free radicals are terminated; this can occur through quenching of primary radicals by oxygen or another inhibitor, through bimolecular termination of two radicals, through reaction of radical-polymer chains with oxygen, or through the trapping of radicals by polymer networks [9].

Thus, there are a large number of possible reactions between the various species present in the reacting mixture. For the purposes of computational modeling, it is necessary to make simplifying approximations and consider only the dominant reactions for each step of the chain reaction. The P-TPL process being modelled [31] uses a mixture of two monomers: pentaerythritol triacrylate (PETA) and bisphenol A ethoxylate diacrylate (BPADA). Since the separate rates of reaction of each monomer are not known, there is no benefit to modeling them as separate species. Instead, a single monomer species is modelled, and the rate of reaction obtained during a calibration step represents a composite rate constant. Similarly, the quenching of primary radicals by oxygen is modelled, but the effect of other inhibitors such as MEHQ is neglected. Since this modelling effort is focused on predicting degree of conversion and not mechanical properties, only addition

polymerization (which increases DOC) is considered, and chain transfer/cross-linking reactions are not explicitly tracked. Finally, since termination by oxygen is the dominant termination mechanism [35], other termination reactions are neglected.

Having made these approximations, the set of chemical reactions for the P-TPL process simplifies to the following:



Equation 1 represents the formation of R^* primary radicals from PI photoinitiator molecules. The P-TPL process under consideration uses a custom photoinitiator that decomposes into two free radicals upon two photon absorption [31]. Equation 2 represents those free radicals that are quenched almost immediately by dissolved oxygen, with the rate of this reaction given by k_q . Equations 3 and 4 are propagation reactions, showing the addition of monomer molecules (represented here as PETA, although also valid if treated as a mix of different monomer molecules) to the primary radical and active polymer chains respectively. Equation 5 represents the termination of the chain reaction when an oxygen molecule reacts with the free radical on a polymer chain to form a dead polymer P^x .

Aside from these chemical reactions, it is also necessary to capture the effect of diffusion processes occurring in the photoresist. While the initial concentrations of the species in the reacting mixture is uniform, the creation of free radicals and subsequent reactions introduce concentration gradients and cause diffusion. For this model, the diffusion of larger molecules is assumed to be negligible. The diffusion of R^* and O_2 is modelled.

For the length scales of P-TPL, a continuum model is more suitable than an atomistic model that models molecules as discrete elements. A continuum model is a higher-level model that operates on species concentrations. Equations 2-5 are first transformed from chemical reactions to a system of differential equations in a manner similar to other works that created reaction-diffusion models of free-radical processes [37].

$$\frac{d}{dt}[R^*] = -k_p[PETA][R^*] - k_q[O_2][R^*] + D_{R^*} \left(\frac{\partial^2[R^*]}{\partial x^2} + \frac{\partial^2[R^*]}{\partial z^2} \right) \quad (6)$$

$$\frac{d}{dt}[PETA] = -k_p[PETA][R^*] - k_p[PETA][P^*] \quad (7)$$

$$\frac{d}{dt}[P^*] = k_p[PETA][R^*] - k_t[O_2][P^*] \quad (8)$$

$$\frac{d}{dt}[O_2] = -k_q[O_2][R^*] - k_t[O_2][P^*] + D_{O_2} \left(\frac{\partial^2[O_2]}{\partial x^2} + \frac{\partial^2[O_2]}{\partial z^2} \right) \quad (9)$$

$$\frac{d}{dt}[R^x] = k_q[O_2][R^*] \quad (10)$$

$$\frac{d}{dt} [P^x] = k_t [O_2][P^*] \quad (11)$$

Equations 6-11 give the rates of reaction, i.e. the rate of change of concentration, of each chemical species. Each of Equations 2-5 is a second-order reaction with the rate of reaction proportional to the concentrations of both reactants, where the proportionality constant is the rate constant k . Thus, they can be written in differential rate law form in the corresponding differential equations. Each term appears in three equations: in the equations for the concentration of each reactant, and in the equation for the concentration of the product. In the former equations, the differential term appears with a minus sign, signifying a decrease in concentration.

Note that Equation 1 was not rewritten as a differential equation. The production of R^* from PI happens at a time scale that is too fast to be accurately captured by a rate constant as used in a numerical reaction-diffusion model with finite time-steps. Instead, this reaction is assumed to be instantaneous, and the concentrations of R^* and PI are changed by the following amount during each pulse:

$$\Delta[R^*] = \frac{D_p \sigma^{(2)} \Phi}{h^2 \nu^2} [PI] \quad (12)$$

Equation 12 models two-photon absorption by the photoinitiator to form free radicals [38]. The amount of PI converted to R^* each pulse is seen to be proportional to the dosage per pulse D_p , which is equal to the intensity squared integrated over the pulse duration. The proportionality constant also includes the previously-discussed two-photon cross-section $\sigma^{(2)}$ and quantum yield Φ . The concentration of [PI] is also tracked and

reduced by one-half of the corresponding increase in R^* each pulse, since each PI molecule forms $2R^*$.

Finally, Equations 6 and 9 also contain spatial derivative terms. These terms come from the diffusion equation, written here in two dimensions in x - z cartesian coordinates. The diffusivity constant D gives the rate of diffusion of each species, while the partial derivative with respect to each spatial dimension gives the concentration gradient in that direction.

2.2 Optical Inputs

While this work is largely focused on chemical modelling, it is nonetheless necessary to have an accurate optics model to predict $\Delta[R^*]$ and subsequent chemical reactions.

Previous work in our group involved the development of a light propagation simulation in MATLAB that predicts the light intensity distribution in the photoresist during a laser pulse [31]. We have also shown that it is possible to initialize a reaction-diffusion model from this intensity distribution, using a simplified version of Equation 12 that assumed an average pulse duration of 35 fs [36]. Since dosage per pulse $D_p = I^2\Delta t$, this is a good approximation if average pulse duration is largely constant while intensity changes.

However, as previously discussed, P-TPL uses temporal focusing that involves modifying the pulse duration as it moves through the photoresist. Thus, we have since updated our optical modeling to model a changing pulse duration as well. The model has

also been updated with the system parameters of our new printing system at Georgia Tech (GT), some of which have changed from the previous system at Lawrence Livermore National Laboratory (LLNL).

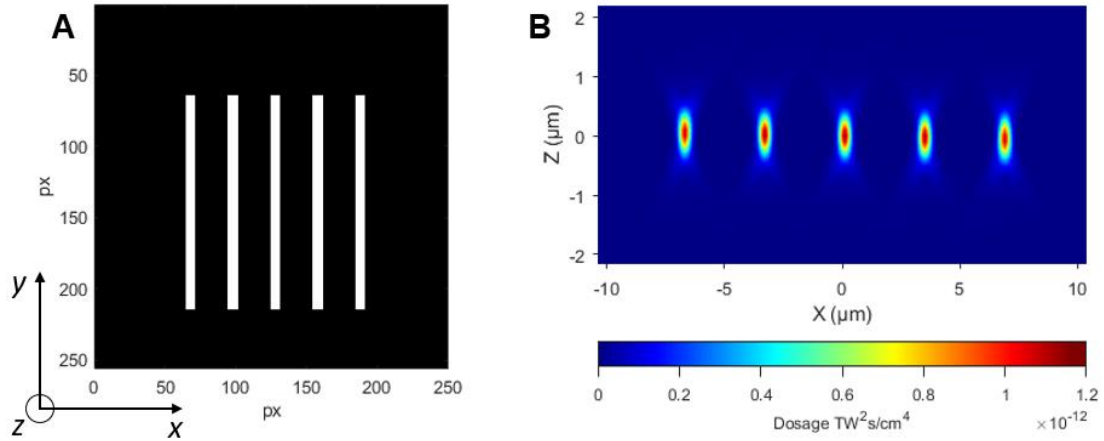


Figure 3: (A) DMD digital mask image (B) X-Z dosage distribution for $y = 0$ plane

Development of the optical model itself was not in the scope of this work but is discussed extensively in the supplementary materials of Saha 2019 [31]. For the purpose of initializing the reaction-diffusion model, the optical model is provided with the digital mask to be applied on the DMD, as well as parameters for the laser power and lens optics. Figure 3A shows an example digital mask for 5 lines of 7px width with 30px spacing. The optical model predicts the dosage delivered to each point in the resist over the course of a single laser pulse. It is then possible to extract the dosage at the desired points for the reaction-diffusion simulation. For instance, a 2D simulation in the $y = 0$ plane of the same five lines is initialized using the dosage distribution in Figure 3B. The cross sections of the five lines are visible.

2.3 Reaction-Diffusion Model Parameters

In addition to the optical parameters, certain chemical parameters and initial conditions need to be determined to set up the model. These parameters are summarized in Table 1.

Table 1: Parameters and Initial Conditions for Reaction-Diffusion Model

Symbol	Parameter Name	Value	Source
$\sigma^{(2)}$	Two-photon cross section of photoinitiator	$133 \times 10^{-50} \text{ cm}^4/\text{s}/\text{photon-molecule}$	Estimate from Rumi et al. (Fig. 5, compound 8) [38]
h	Planck's constant	$6.626 \times 10^{-34} \text{ m}^2 \text{ kg} / \text{s}$	Fundamental constant
k_p	Polymerization rate constant	$4.3 \times 10^4 \text{ dm}^3 \text{ mol}^{-1} \text{ s}^{-1}$	Mueller et al. [35]
k_q	R* quenching rate constant	$2.3 \times 10^6 \text{ dm}^3 \text{ mol}^{-1} \text{ s}^{-1}$	
k_t	Termination rate constant	$5.9 \times 10^4 \text{ dm}^3 \text{ mol}^{-1} \text{ s}^{-1}$	Calibrated against empirical data
Φ	Quantum yield of photoinitiator	0.0061	
DOC_{th}	Degree of conversion threshold	0.068	Determined through micro-Raman spectroscopy
D_{O_2}	Diffusivity of oxygen	$1.2 \times 10^{-12} \text{ m}^2 \text{ s}^{-1}$	Estimated using Stokes-Einstein equation
D_{R^*}	Diffusivity of R*	$10^{-13} \text{ m}^2 \text{ s}^{-1}$	

Table 1 Continued

Symbol	Parameter Name	Value	Source
ν	Optical frequency (central)	375 THz	Properties of laser in the printer
	Pulse repetition rate	5 kHz	
$[\text{O}_2]_0$	Initial O_2 concentration	$6 \times 10^{-3} \text{ mol dm}^{-3}$	Mueller et al. [35]
$[\text{PI}]_0$	Initial photoinitiator concentration	$1.65 \times 10^{-3} \text{ mol dm}^{-3}$	Resist composition, PI at 0.1% by weight
$[\text{PETA}]_0$	Initial monomer concentration	4.0 mol dm^{-3}	Material datasheet for PETA [39]
$[\text{R}^*]_0$ $[\text{P}^*]_0$ $[\text{R}^x]_0$ $[\text{P}^x]_0$	Initial values of other species' concentration	0 mol dm^{-3}	No light exposure and no reacting species present at $t = 0$

While most parameters are set using literature sources or based on the physical model setup, certain parameters needed to be calibrated or experimentally determined due to a lack of existing data on them.

2.3.1 Calibration Scheme

The parameters k_t and Φ were set by calibration of the model to a set of experimentally collected data. Using the version of the Nelder-Mead simplex method [40] implemented in MATLAB's `fminsearch()` function, the two parameters were set through an optimization routine. At each optimization step, the model was solved for a projection

of 5 lines printed with two different exposures. The width of the lines was measured experimentally through scanning electron microscopy and the error in the line widths predicted by the simulation was calculated. The optimization routine was allowed to change k_t and Φ while attempting to minimize the error. The optimized values of k_t and Φ were found to predict the printed line width to within the precision of the simulation measurements.

2.3.2 *Experimental Determination of DOC_{th}*

The threshold degree of conversion at which the polymer becomes insoluble was determined experimentally for the resist mix used in the printing setup. Macroscopic droplets of Irgacure 651 photoinitiator were added to the PETA/BPADA resist used in P-TPL printing. The droplets were exposed to flood UV illumination of fixed intensity for various durations of time. The droplets were then treated using the same development process used for newly-printed P-TPL samples by submerging them in propylene glycol monomethyl ether acetate (PGMEA) for 10 minutes and then in isopropanol for 10 minutes. This development process is known to wash away polymer with $DOC < DOC_{th}$. Thus, it was possible to determine the exposure necessary to just achieve the threshold DOC. Under the conditions of the experiment, this time was found to be 10 minutes, as shown in Figure 4. For exposures smaller than this, the development process washed all printed polymer off the slide.

Having identified the threshold sample, the DOC was then measured using Raman microspectroscopy, a technique that has been successfully applied on TPL prints previously [40]. A Renishaw inVia Qontor Raman micro-spectroscope was used with a

785 nm wavelength laser and a 1200 lines/mm diffraction grating. The samples were exposed to the Raman beam for 10 seconds at 5% of the laser power. DOC was measured at different points through the droplet and the value at the surface, corresponding to the lowest observed DOC, was used.

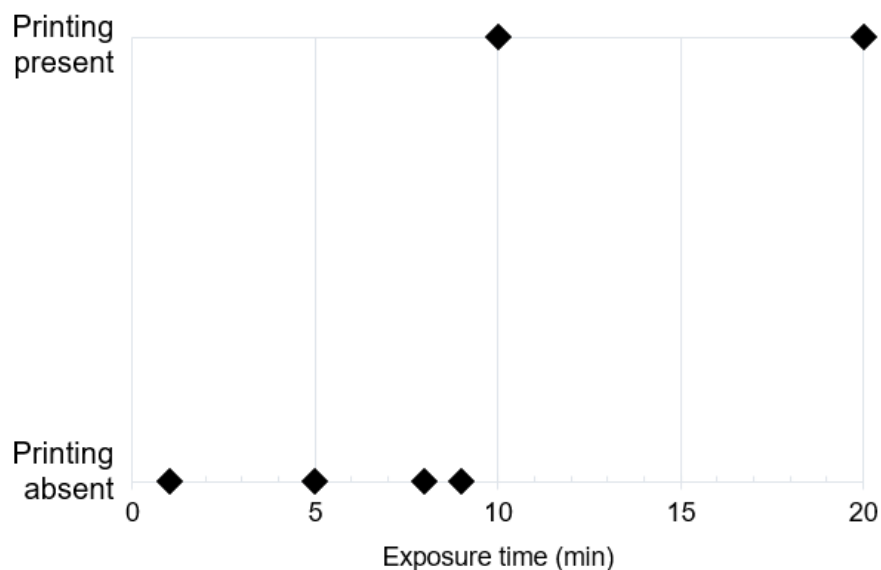


Figure 4: Presence or absence of printing for different exposure durations

The concentration of a bond is given by the area under the corresponding peak in a Raman spectrogram such as in Figure 5. Since different bonds produce Raman signals at different wave numbers, Raman spectrograms can be used to calculate the relative proportion of C=O and C=C bonds in the sample. The absolute DOC can be determined by comparing the change in this proportion before and after the sample was exposed to U.V. light, since the number of C=O bonds does not change during polymerization. In equation form, this is represented as:

$$DOC = 1 - \left(\frac{A_{C=C}/A_{C=O}}{A'_{C=C}/A'_{C=O}} \right) \quad (13)$$

where $A_{C=C}$ and $A_{C=O}$ represent the areas under the peaks of the post-exposure Raman spectrogram, and $A'_{C=C}$ and $A'_{C=O}$ represent the areas under the corresponding peaks for the pre-exposure Raman spectrogram [32]. In this manner, the DOC of the threshold sample was measured to be 6.8%, and this is the value used as DOC_{th} .

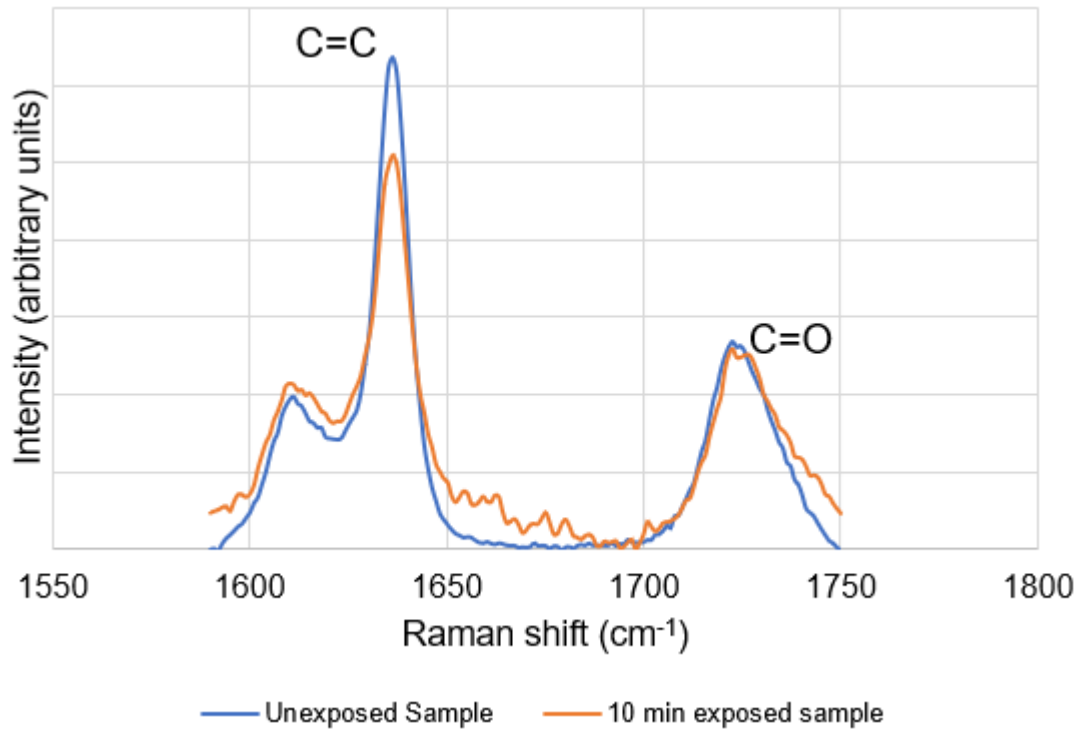


Figure 5: Raman spectrogram for exposed and unexposed sample

2.4 Finite Element Modeling in COMSOL

A reaction-diffusion model solves a set of equations such as Equations 6-12 to predict the evolution of the concentrations of various species in the reacting system. Since these reactions need to be solved for arbitrary geometries with potentially non-uniform initial and boundary conditions, they must be solved numerically rather than analytically. Thus, the equations were programmed into COMSOL Multiphysics, a commercially available finite element analysis software package that can solve arbitrary PDE systems. The implementation of both 2D and 3D geometries is described in this subsection.

2.4.1 2D Model

In two dimensions, the model represents an x - z plane, since for a typical TPL print such as nanowires, simulating this plane gives predictions about the cross-section, such as the predicted width and height of a nanowire.

For nanowire simulations, the geometry used is a $30\ \mu\text{m} \times 10\ \mu\text{m}$ rectangle as shown in Figure 6. A mapped mesh with finer elements in the central region where printing occurs is used. Each element is a rectangle using quadratic Lagrange shape functions. Mesh convergence was performed with the DOC being the output variable of interest. The mesh was found to converge at $n = 40$ for most printing regimes, such as the one studied in Figure 7, with finer meshes only required in especially challenging chemical parameter regimes.

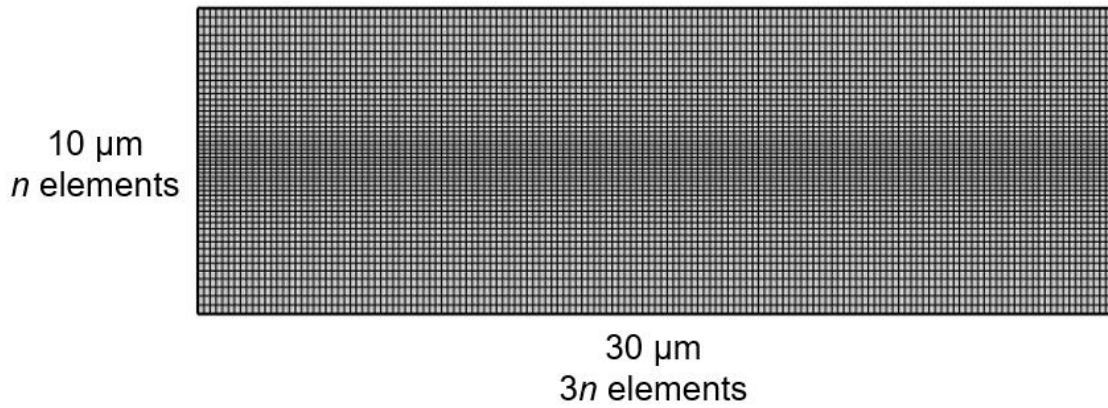


Figure 6: 2D model geometry and mesh

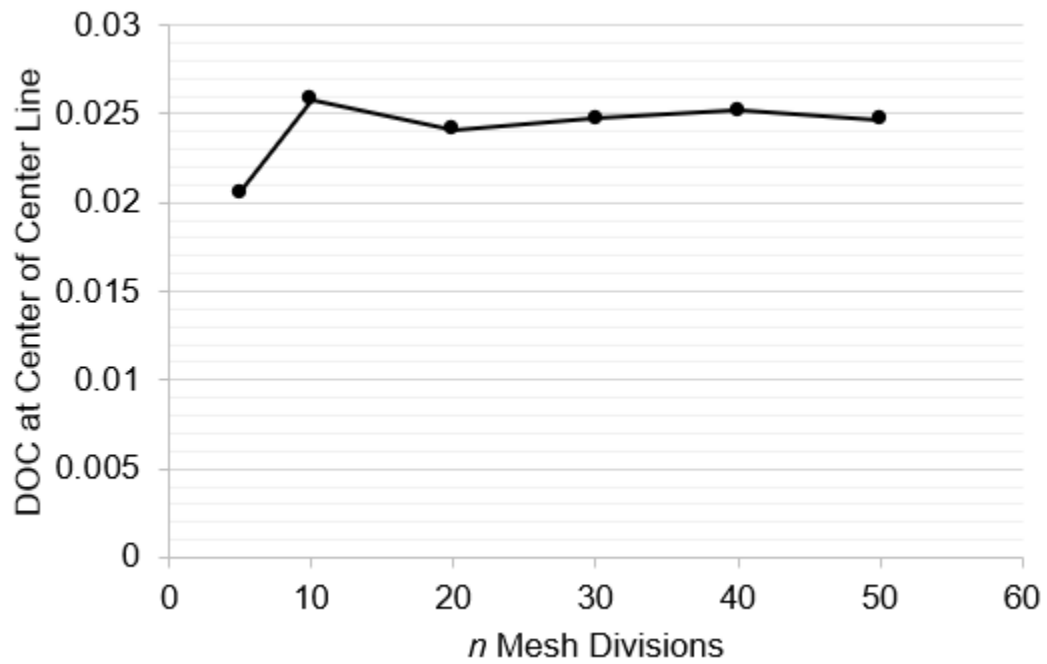


Figure 7: Mesh convergence for 2D model. Simulation of five 3 px lines with 1.2 ms exposure.

The PDE system was implemented using COMSOL's Coefficient Form PDE interface, as the standard chemical engineering interfaces did not offer enough flexibility to represent the P-TPL process accurately. Dirichlet boundary conditions were used to hold the value of O_2 constant at O_{2-0} , representing the abundance of O_2 sufficiently far from the print. Initial conditions were set as described in Table 1.

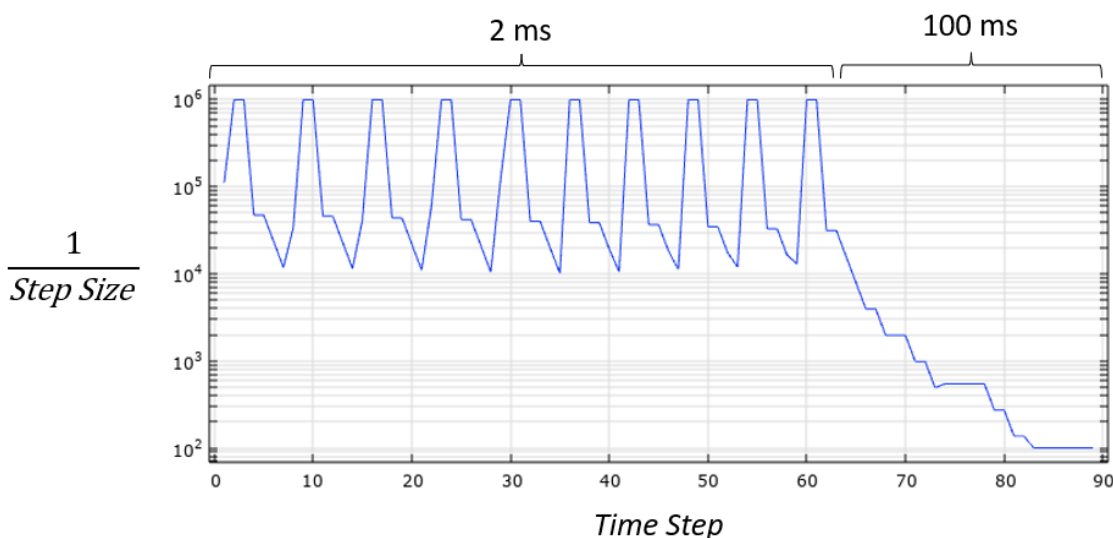


Figure 8: Solver time step size over the course of a model solve.

The model was solved using a time-dependent direct solver, since it was desired to track the temporal evolution of species concentrations. The PARDISO solver was found to give the best performance. It was necessary for the model to handle both extremely small time scales in the vicinity of the laser pulses, and much longer time scales of up to 1 second during the post-exposure dark period. COMSOL's Events interface was used to handle this multiscale modeling by forcing the solver to take smaller time steps only near laser pulses, where reaction rates are likely to be higher, while allowing the adaptive time-stepping algorithm to choose larger time steps elsewhere as appropriate. The effect of this is shown in Figure 8, which shows a model solved for 10 pulses over the course of 2 ms, followed

by a 30 ms dark period. The step size is seen to be several orders of magnitude smaller in the “peaks”, representing the pulses, and much larger between pulses and especially in the dark period, which takes relatively few steps despite being 50x the length of the exposure in simulation time.

The Events interface also allows for the dosage per pulse to be added pseudo-instantaneously, representative of the femtosecond timescales of the laser pulses. The dosage at each point is found by interpolating from the results of the optical model described earlier. Instead of actually slowing the solver down to femtosecond time-steps, other reactions are paused while $[R^*]$ is increased and $[PI]$ is decreased over a time on the order of microseconds, thus achieving in effect an instantaneous addition of R^* but without requiring extremely high tolerances.

2D model solve times were observed to be on the order of a few minutes, with the exact solve time depending on the simulation conditions, particularly the length of exposure. The exposure, dark period, and other parameters can be varied as desired to perform parametric sweeps.

The output of the model solve is data for concentration of each chemical species at each point in space and time. The DOC is calculated from the concentration of PETA using Equation 14.

$$DOC = 1 - \frac{[PETA]}{[PETA]_0} \quad (14)$$

Figure 9 shows an example of DOC profiles at different times, once again with a simulation of the cross-sections of 5 parallel lines. The DOC is zero everywhere at the start of the simulation and increases as the reaction progresses, eventually reaching a steady-state value where the maximum DOC is 0.12. In this printing regime, the DOC profile takes roughly the same shape as the dosage distribution in Figure 3, indicating minimal diffusion effects. Later in this work, the regimes in which diffusion is active will be investigated.

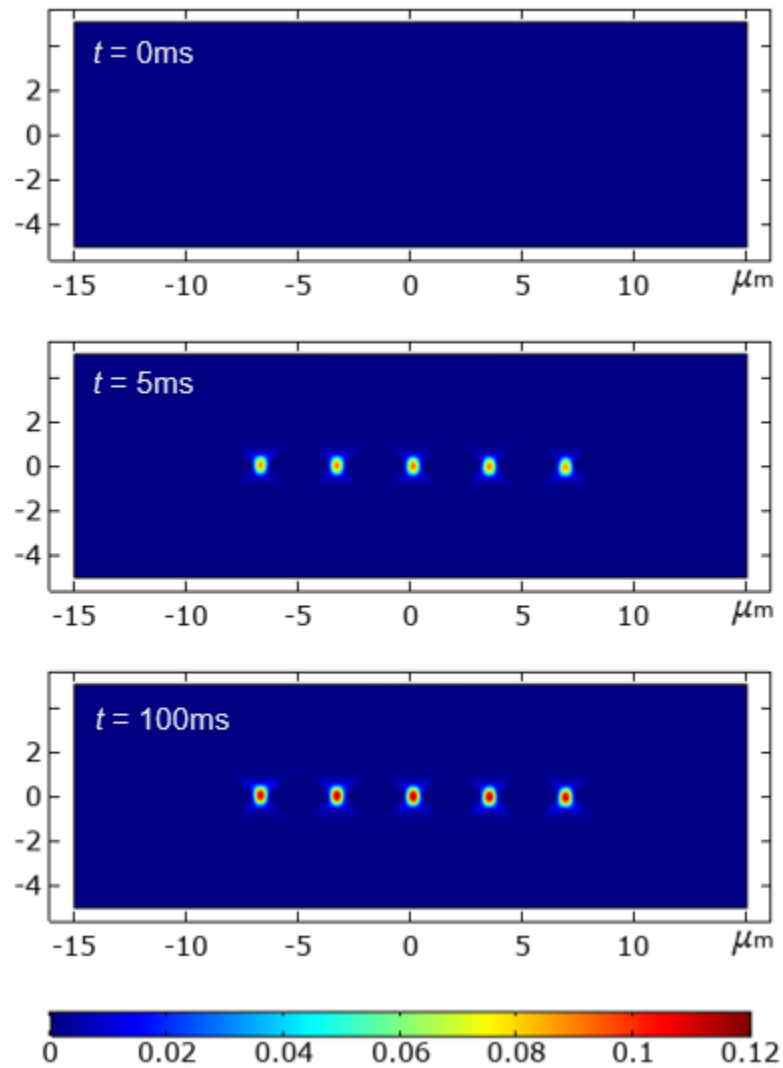


Figure 9: Degree of conversion profile at different times

Alternatively, the simulation result can be visualized by tracking species concentrations at a single point; Figure 10 does this for the center point of the center line, which is the point that reaches the highest DOC. R^* peaks corresponding to each laser pulse are seen; these are rapidly quenched or converted to P^* . As photoinitiator is consumed, the heights of successive R^* peaks are seen to decrease. The DOC is seen to continue to increase well into the dark period, before eventually reaching steady-state at around 10 ms. The rate of oxygen diffusion is much less than the rate of oxygen consumption by the quenching and termination reactions, and oxygen is not substantially replenished while the reaction is active.

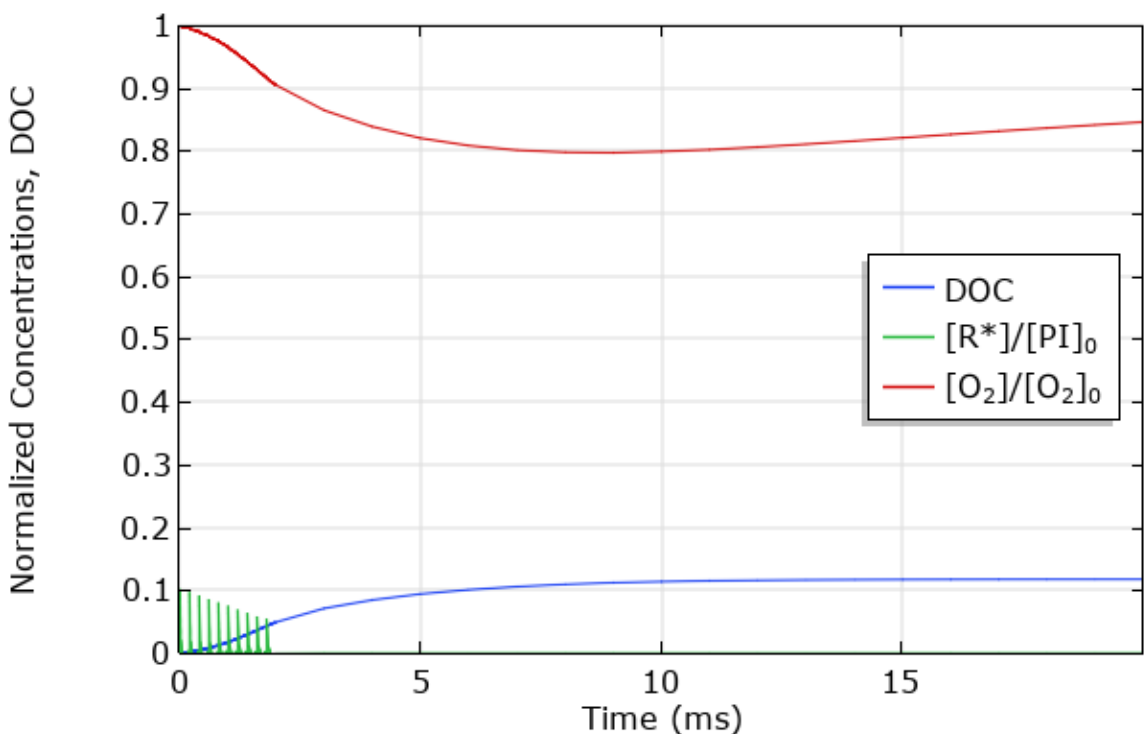


Figure 10: DOC, $[R^*]$ and $[O_2]$ at the center of the center line

In order to measure print dimensions, the threshold DOC was applied to convert the DOC range into a binary outcome of printing or no printing. Regions with $DOC > DOC_{th}$ were considered printed, as shown in Figure 11. Height and width were measured on the central axes.

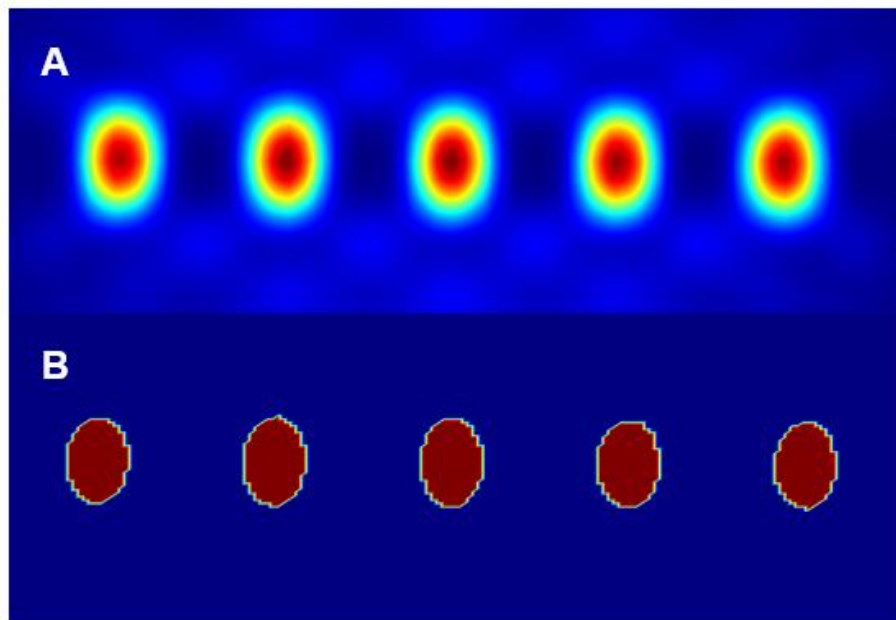


Figure 11: A: DOC. B: $DOC > DOC_{th}$

A previous version of the model was validated against experimental data collected at the P-TPL printing setup at Lawrence Livermore National Laboratory, as part of a published investigation into P-TPL feature size prediction [36]. Predicted and experimentally measured nanowire heights and widths are plotted in Figure 12. While feature size predictions are comparable to experimental results, an inaccuracy in predicted aspect ratios is noted. Further improvements to the computational model were implemented after collection of this dataset.

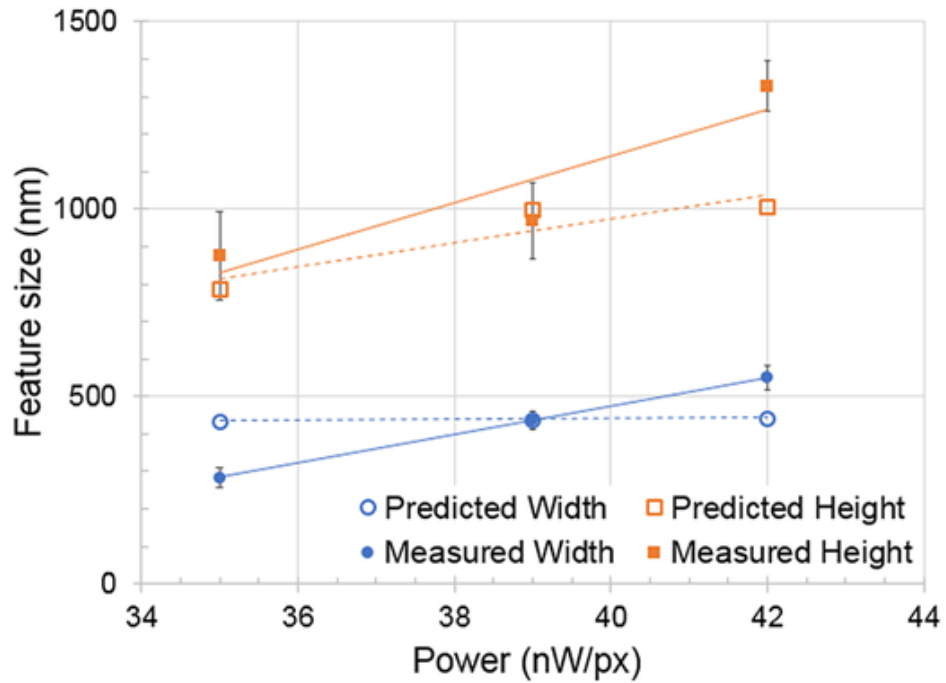


Figure 12: Predicted versus measured nanowire widths and heights for different beam powers [36]

2.4.2 3D Model

The setup for the 3D model was identical to that of the 2D model with the exception of the geometry. The 3D geometry used was of the form shown in Figure 13. The simulated volume is smaller due to the increased computational cost of a 3D model. Meshing and mesh convergence were performed similar to the 2D model, with the data plotted in Figure 14 showing that mesh convergence is attained at 28 mesh divisions.

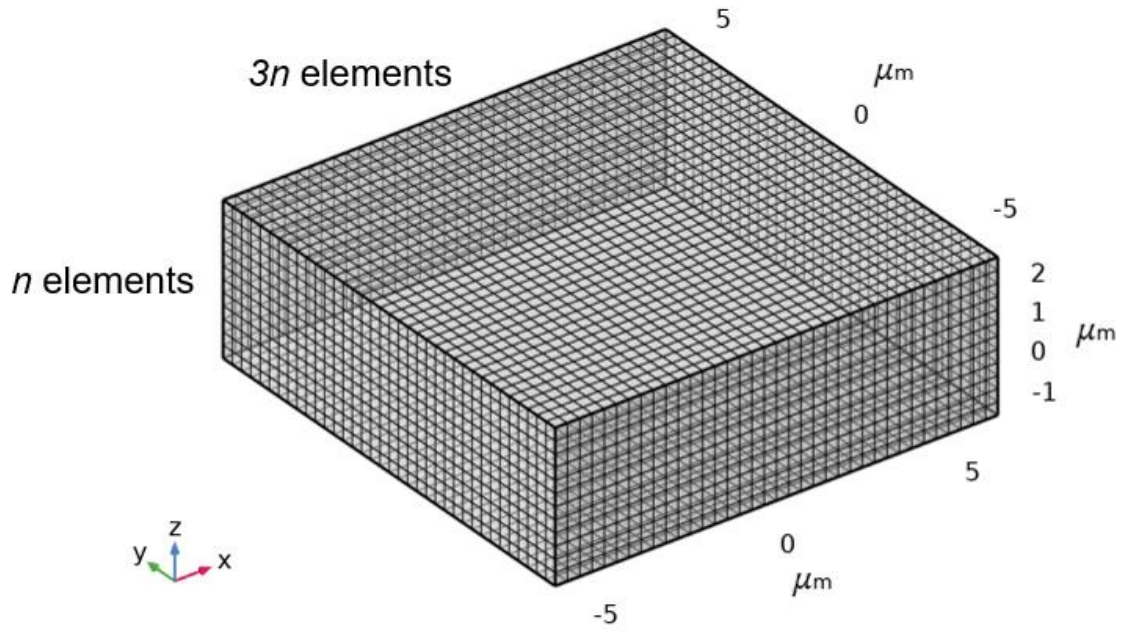


Figure 13: 3D model geometry and mesh

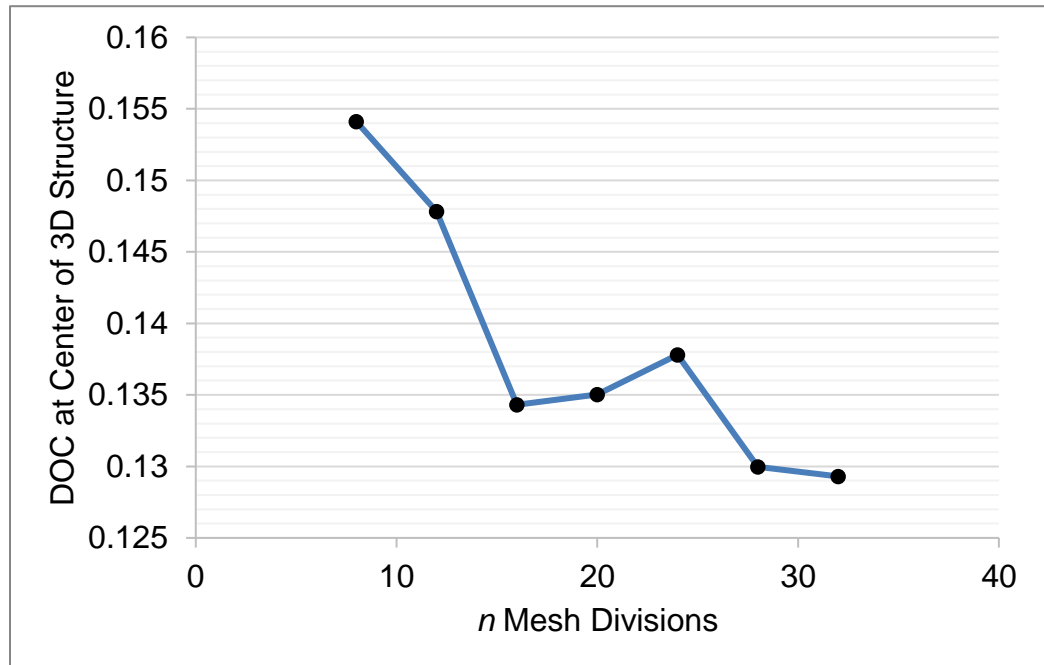


Figure 14: Mesh convergence for 3D model. Simulation of log-pile structure depicted in Figure 15.

Since the 3D model allows for diffusion of R^* and O_2 in the y - direction in addition to x - and z -, it is suitable for simulation of prints that contain both in-plane and out-of-plane geometric features. One example of such a print is a log-pile structure with lines alternately oriented in-plane and out-of-plane, which cannot be captured by a single 2D model. The results from the 3D simulation are shown in Figure 15, with regions above the threshold DOC displayed. The distinctive layer-by-layer construction of P-TPL-fabricated structures is evident.

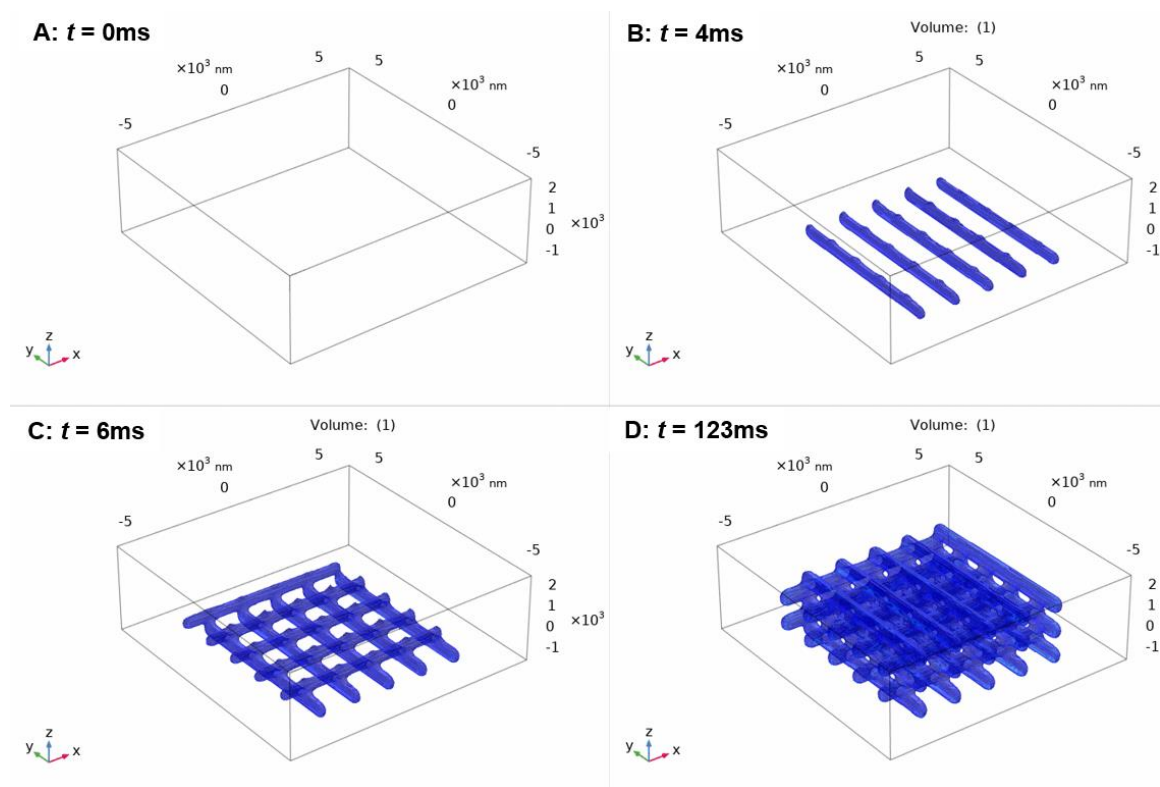


Figure 15: 3D model results, printed region at different times

Solve times for converged 3D models were substantially longer due to increased mesh connectivity compared to the 2D model, approaching 24 hours for fully converged solutions when running on a computer with an Intel® i7-9700K CPU and 64 GB of RAM. As Figure 16 demonstrates, increased 3D mesh connectivity leads to greater solve times for the same number of degrees of freedom. This is an unfavorable trend that cannot be resolved by simply simulating smaller volumes to keep the degrees of freedom the same as in 2D.

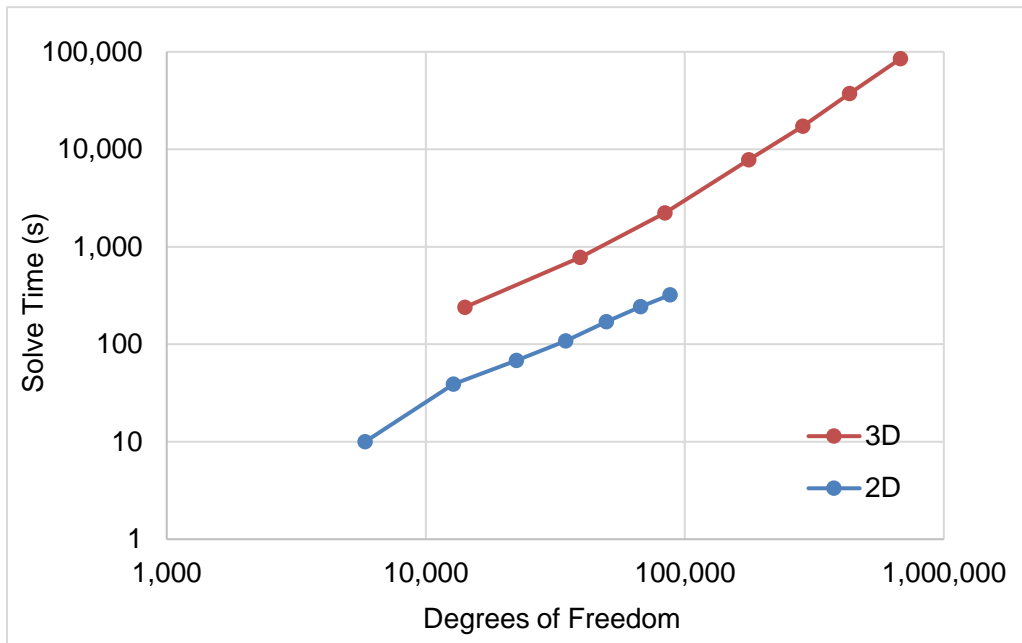


Figure 16: Solve time vs. degrees of freedom for 2D and 3D models, 50 pulses.

However, it was found that under the high O_2 , low diffusion environment of the parameters in Table 1, the error in using a 2D instead of 3D model was minimal. For instance, Figure 17 shows a comparison of a 2D and 3D simulation of a five line print. The cross-section predicted by the 2D model is almost identical to that found by the 3D model

that simulated the whole length of the line. Thus, for the rest of this work, the 2D model is used for data collection and experiments are limited to parallel lines.

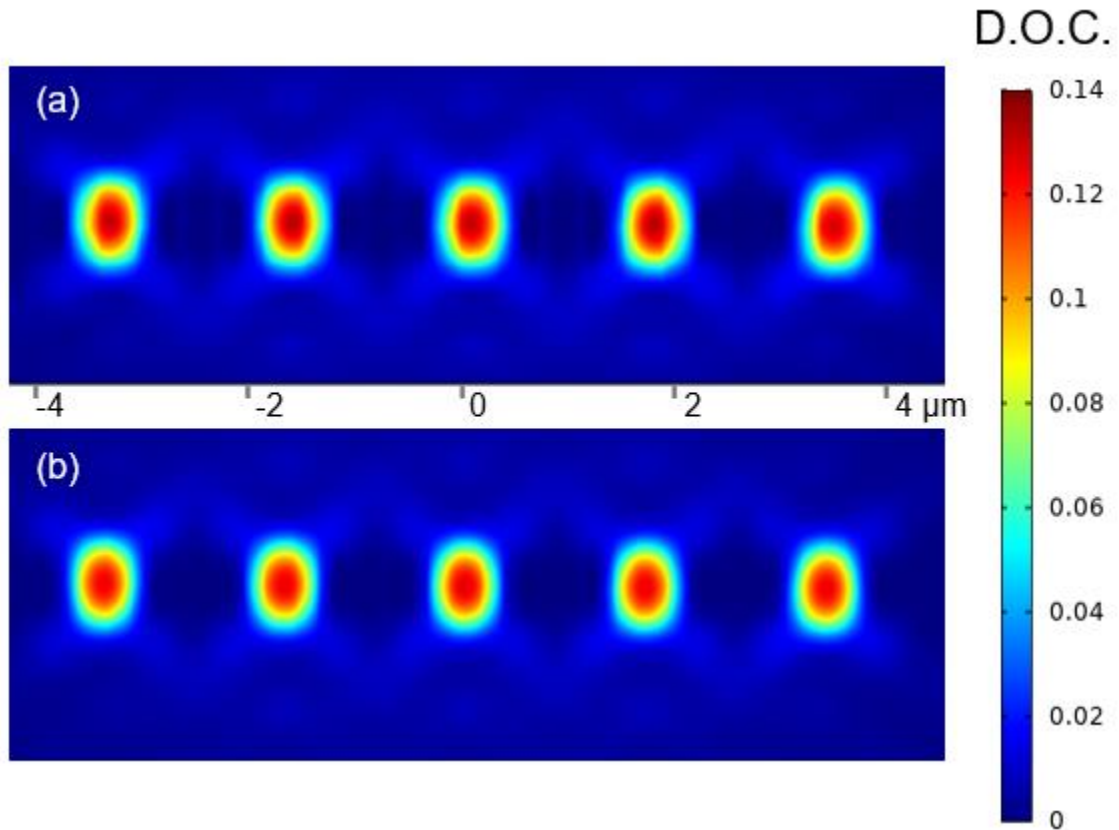


Figure 17: Degree of Conversion for simulation of 5 parallel lines after 10 pulse exposure, $y = 0$ plane (a) from 3D model (b) from 2D model

CHAPTER 3. NEURAL NETWORK SURROGATE MODELING

So far, we have developed a high-fidelity model capable of simulating P-TPL printing outcomes with a relatively high degree of accuracy. However, even with the optimizations discussed so far, the reaction-diffusion model is computationally expensive to solve. In particular, parametric studies that vary parameters other than exposure cannot benefit from the dynamic programming optimization discussed in Appendix A.2 and will take significantly longer to solve, making studies of tens to hundreds of thousands of parameter combinations impractical. Such studies are of interest when moving beyond the calibrated conditions we have worked with so far. Moving to a different photoresist or photoinitiator, for example, will lead to different rate constants, quantum efficiency, DOC threshold etc. Being able to reliably predict printing outcomes across the design space is essential for a computational model to be generalizable and not limited to a bespoke system.

In this chapter, surrogate modeling techniques to solve the problem of developing a computationally cheap method to evaluate approximate solutions across large parameter spaces rapidly. Surrogate modeling or metamodeling refers to the practice of developing a “model of a model” by simplifying, sampling and regressing, or otherwise approximating the original high-fidelity model [41]. Surrogate models trade off accuracy for faster compute time, and are therefore suitable for problems where speed is critical.

Artificial Neural Networks are an increasingly common choice of surrogate modelling method [41]. A Neural Network (NN) is a machine learning method that acts as a black box and “learns” the input-output relationship of the data it is trained on. An NN

typically consists of many nodes, each somewhat analogous to a neuron in the human brain. Each node transforms the data into it using some mathematical operation, and then outputs it to the next node. The nodes are organized into layers that operate at once; a neural network can contain thousands of such layers. In a classification neural network, the output of the final layer is transformed into a categorical value, allowing for the NN to be used in classification applications. The NN must first be trained, typically using a backpropagation algorithm that adjusts weights of intermediate nodes by computing the error in predicted output and propagating it backwards through the neural network [42].

3.1 Training Data Set Collection

For the purpose of this application, a shallow neural net of only a few layers was trained to classify printable regions [43]. Print results were classified as no printing (class -1) when there was no polymer above the threshold DOC, as shown in Figure 18A. The desired outcome was the normal printing (class 0) shown in Figure 18B. In Figure 18C the print is classified as overprinted (class 1) due to the overpolymerization and merging of lines.

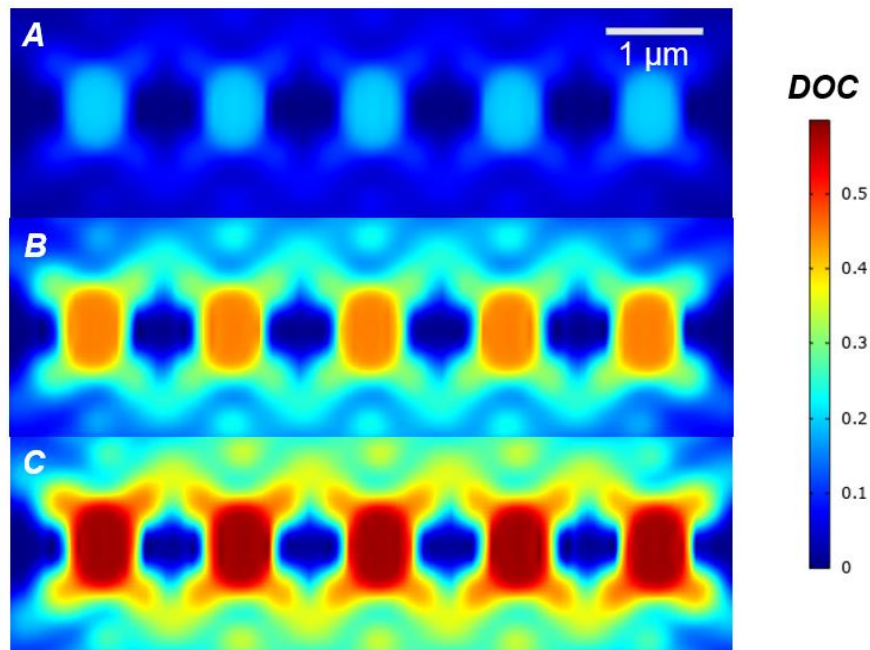


Figure 18: Printing Outcomes: A) No Printing B) Printing C) Overprinting

Training a neural network for a high dimensional parametric space with large parameter ranges requires an extensive set of training data. In the case of a surrogate model, this data can be generated from the parent simulation. The parameter ranges that were studied are shown in Table 2. Wide ranges of rate constants, quantum yields, and solubility thresholds were chosen to represent as many different photoresists as possible. The parameters A and B control the exponential decay of the rate constants k_p and k_t respectively as DOC increases, thus modeling the slowing of the reaction as polymerization progresses and chemical diffusion and reactions are hindered.

Table 2: Neural Network Data Collection Parameters

Parameter	Lower Bound	Upper Bound	Units
k_{p-0}	1	1×10^8	$\text{dm}^3 / \text{mol} / \text{s}$
k_q	1	1×10^8	$\text{dm}^3 / \text{mol} / \text{s}$
k_{t-0}	1	1×10^8	$\text{dm}^3 / \text{mol} / \text{s}$
Number of pulses	1	20	1
A	1×10^{-20}	1×10^{-10}	1
B	1×10^{-20}	1×10^{-10}	1
Power	0.01	0.50	W
Φ	1×10^{-4}	1×10^{-2}	1
$[\text{PI}]_0$	1×10^{-4}	1×10^{-2}	mol/dm^3
DOC_{th}	0.02	0.70	1

Constructing a full factorial dataset requires k^n datapoints where k is the number of levels per parameter and n is the number of parameters. With 10 parameters, the required number of datapoints becomes impractical even for modest values of k . Thus, a different choice for the design of the experiment was made and Latin Hypercube Sampling (LHS) was chosen for its ability to produce a representative sampling of the parameter space given only n sample points. LHS works by dividing the range of each parameter into n intervals

and placing a point randomly within each interval [44]. Combinations of points from each parameter are created at random to generate the full parameter matrix. The value of n can be chosen based on what is feasible for the experiment, and is independent of the number of dimensions. In contrast to random Monte Carlo sampling, LHS guarantees sampling that is representative of the parameter space. In this case, LHS was implemented using MATLAB's `lhsdesign()` function to generate a parameter matrix for COMSOL.

The parameter ranges in Table 2, particularly the rate constants, span many orders of magnitude. In order to not waste compute time on sampling vast parameter spaces that did not generate any printing, the simulation experiment was performed in batches, using the results from previous batches to discard regions appearing to be totally unprintable so as to focus computational time on generating as many sample points as possible near printable regions. Simulation was performed in parallel on a computing cluster. More details on the use of High Performance Computing (HPC) for the collection of this dataset can be found in Appendix A.1.

Through the use of HPC, 7084 2D simulations were completed. Data augmentation was used to increase the size of the training dataset further. Since the underlying physics of Equations 6-12 was the same for all simulations, it was possible to determine which parameters in Table 2 were positively correlated with printing (e.g. $k_{p-\theta}$, Φ) and which were negatively correlated (e.g. k_t , k_q). Then, it was possible to generate synthetic datapoints by extrapolating: if a given parameter combination results in overprinting, then any parameter combination where the parameters positively correlated with printing are increased and the parameters negatively correlated with printing are decreased will also result in printing, and vice-versa for datapoints with no printing. In this manner, a larger dataset of 26,769

points was generated without significant computation, an increase of almost four times over the original. It should be noted that this data augmentation procedure only works for classification applications (printing, overprinting, no printing); it is not viable when the actual degree of conversion or print dimensions need to be measured.

3.2 Neural Network Design and Performance

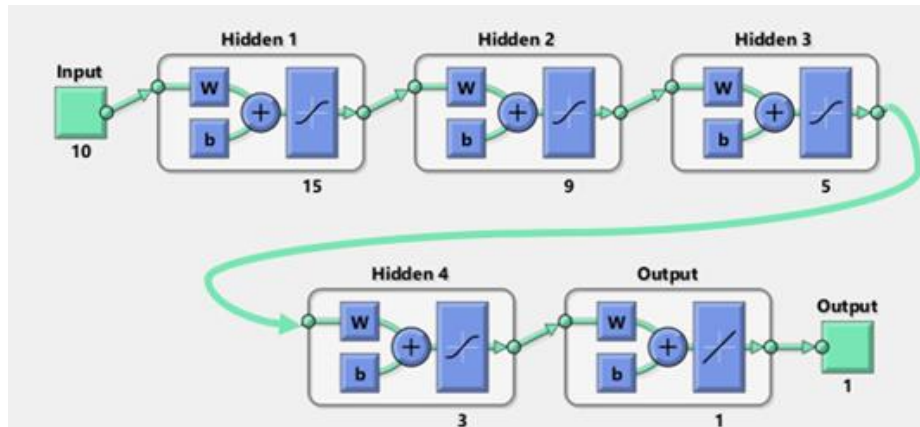


Figure 19: Neural Network Structure [43]

The neural network was trained in MATLAB using the `fitnet()` function from the Statistics and Machine Learning Toolbox. `fitnet()` is suitable for rapidly training classification NNs. Inputs to the NN were treated as numerical values, as were outputs (-1, 0, 1 corresponding to no printing, printing, overprinting). After experimenting with various different layer sizes and numbers, 4 layers of sizes 15, 9, 5, and 3 were chosen, as shown in Figure 19. The rectified linear unit (ReLU) activation function was utilized for the hidden layers. The softmax activation function was utilized for the output layer. Training was done on a computer with an Intel® i7-1165G7 processor and 16GB of RAM and took an average of 4 minutes. To avoid overfitting, 5-fold cross-validation was then performed.

15% of datapoints were reserved for testing. The trained NN was found to predict the correct printing outcome as given by FE simulation 98.1% of the time [43]. The confusion matrix in Figure 20 breaks down this performance further. The average time taken to interrogate the NN for a given set of parameters was 0.32 μ s. It is this near-instantaneous solve time that allows for rapid evaluation of thousands to millions of datapoints, enabling studies such as the one in Chapter 4

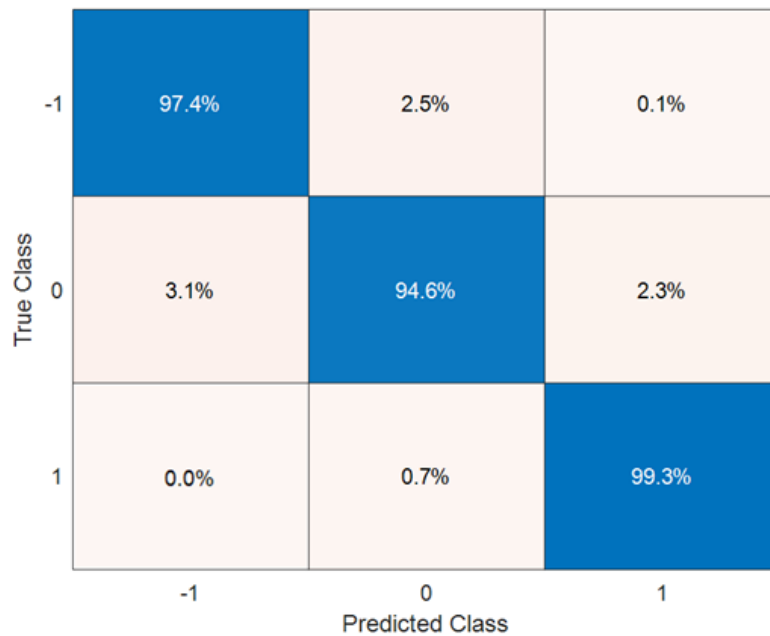


Figure 20: Confusion Matrix for Neural Network Results [43]

CHAPTER 4. EXPERIMENTS, RESULTS, AND DISCUSSION

Having developed two computational models of P-TPL, one optimized for accuracy and the other for speed of evaluation, we can now proceed to investigate the process limits whose characterization is the goal of this thesis. In this chapter, defects from proximity effects, resolution limits, and printability regimes are investigated.

4.1 Investigation of Proximity Effects

Proximity effects, where the printing of features deviates from the projected image due to the influence of neighboring printing, are important to characterize and compensate for. It is hypothesized that proximity effects are more significant in P-TPL than in serial TPL, since the layer-by-layer projection results in active chemical reactions across a large area at the same time. In this section, the reaction-diffusion computational model is used to investigate proximity effects arising from the chemistry of TPL. The ability of P-TPL to overcome the proximity effect and print porous structures is explored.

Diffusion is the relevant process that allows for a proximity effect due to chemical reactions. We have previously considered O_2 and R^* to be diffusing species; in this section we focus on tracking O_2 , since Table 1 assigns it a diffusivity an order of magnitude higher than R^* . Simulations were performed for a projection of five 5-pixel wide lines and an exposure of 3.2 ms (16 pulses).

Figure 21A tracks the evolution of chemical species concentrations at the center of the center line when the simulation is run under the nominal conditions given in Table 1. The amount of $[P^*]$, which can be thought of as accumulated dosage, is seen to rise linearly

during the exposure period before decaying exponentially during the dark period. Oxygen is seen to be replenished during the dark period through diffusion; the photoresist remains relatively oxygen-rich throughout the reaction, even at this center point that receives the highest optical dosage.

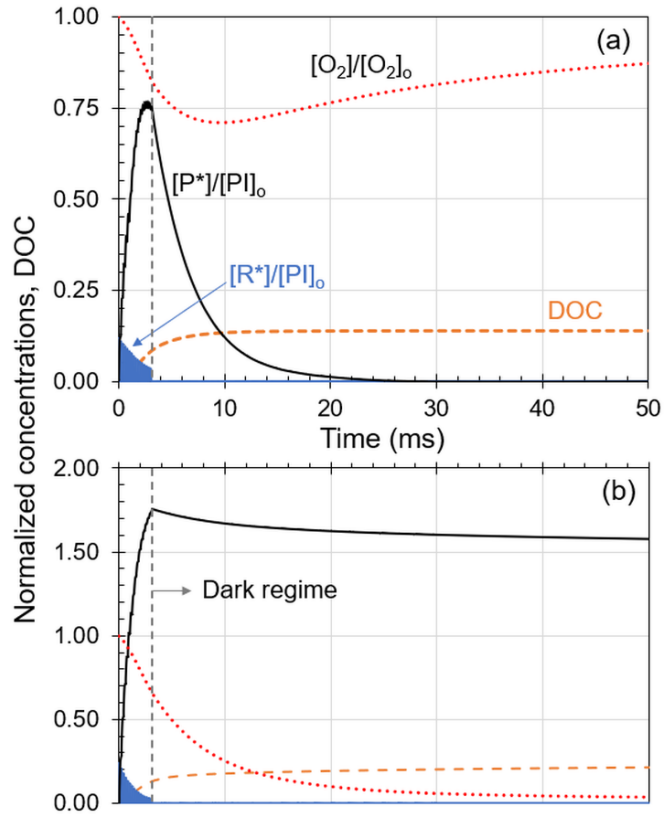


Figure 21: Temporal evolution of chemical species concentration at center of center line for a projection of 5 x 5 px lines (a) normal O₂ (b) 5% of normal O₂

For comparison, a second simulation was run with an artificially low O₂ concentration. Results are plotted in Figure 21B. As expected, a larger accumulation of dosage and resulting degree of conversion are seen. (The maximum obtainable value of $[P^*]/[PI]_0$ in P-TPL is 2, since each PI produces two R*, which convert to P* if not

quenched by O₂.) Furthermore, the diffusion of O₂ from surrounding areas is seen to be very slow.

Figure 22 visualizes the profile of O₂ concentration moving away from the center of the line in both axial and lateral directions. Figure 22C and D show these profiles for various times after printing in the low O₂ environment, providing evidence for flat concentration gradients that result in timescales on the order of seconds to replenish O₂ through diffusion. Figure 22A and B show the regular O₂ environment. The limit of diffusion effects for these conditions is seen to be about 500 nm in the lateral direction and about 750 nm in the axial direction.

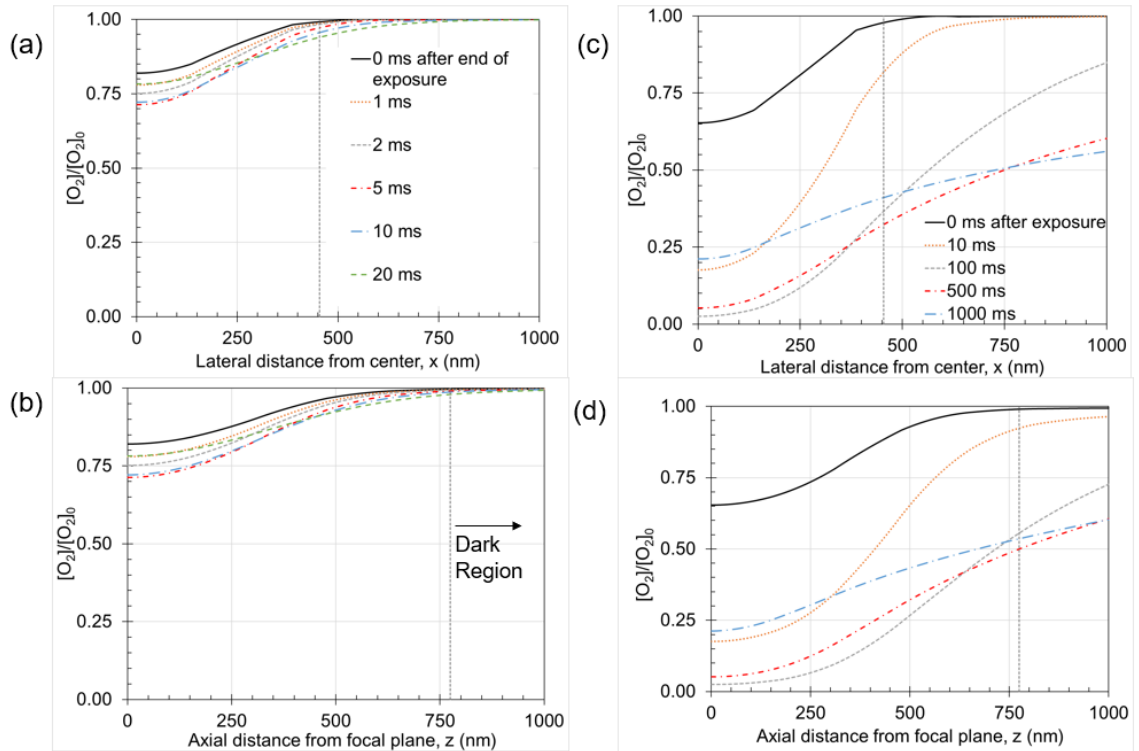


Figure 22: O₂ drop off from the center of the center point in lateral and axial directions, various times. (a) and (b) for normal [O₂], (c) and (d) for 5% of normal [O₂]

Taken together, these observations provide evidence for the idea that printing under relatively oxygen-rich conditions, where the concentration of primary radical generated is low compared to the background concentration of O₂. These conditions can be achieved through the control of exposure, projection, power, and photoinitiator concentration. Printing that consumes relatively small amounts of oxygen induces smaller concentration gradients, which means lower diffusion and proximity effects. That is, less oxygen is depleted from surrounding regions, so future printing nearby does not result in overpolymerization. Since P-TPL can print features with fewer pulses than serial TPL, owing to its layer-by-layer projection scheme and slower laser repetition rate, it is easier to achieve conditions with lower oxygen consumption. Post-print curing can be used to increase the DOC after printing if desired for improved mechanical properties [32].

4.2 Investigation of Resolution Limits of Nanowire Printing

Next, a study can be conducted to investigate the resolution limits of P-TPL printing of nanowires under calibrated conditions. For any projected line width and power, there is a threshold exposure required to reach the threshold DOC and achieve printing. However, since the exposure depends on a discrete variable (number of pulses), it is not possible to print arbitrarily fine structures simply by reducing the exposure to just above that required to achieve DOC_{th} .

Thus, delivering only the minimum necessary dosage to achieve DOC_{th} in a printing set up where only the projection and exposure can be varied is a non-trivial problem. It is hypothesized that a combination of projections of varying linewidths could give finer

exposure control and thus allow for higher resolutions than are achievable by varying the exposure on a single projection.

An experiment was devised to investigate this hypothesis by running simulations of two superimposed projections with varying exposure and gap between them. Table 3 shows the parameter ranges studied. All projections were of 5 lines of 30 px period, with a laser power of 89 mW, simulated in the x - z plane using the 2D reaction-diffusion simulation. A dark period of 100 ms was added after the final exposure. Other parameters were held constant at the values given in Table 1.

Table 3: Multiple Projection Experiment Parameters

Parameter	Values
Projection 1 width	3px, 5px, 7px
Projection 1 exposure	1 pulse - 40 pulses
Gap between projections	0ms, 2ms, 4ms, 6ms, 8ms, 10ms
Projection 2 width	3px, 5px, 7px
Projection 2 exposure	1 pulse - 40 pulses

The use of simulation enables the study of large numbers of parameter combinations in a manner that cannot be achieved experimentally. However, the large number of possible combinations in this experiment still poses challenges. With just the five parameters in Table 3, there are $3 \times 40 \times 6 \times 3 \times 40 = 86,400$ combinations.

Solving this number of simulations serially would require many months of computation. Furthermore, the surrogate modeling approaches discussed in the next chapter are not appropriate for a problem that requires precise measurement of line width and height.

To enable solving of this problem, various high-performance computing scripts were written. A full discussion of these tools can be found in Appendix A.2. For the purpose of this experiment, HPC enabled parallel computation of 100+ models using Georgia Tech's Partnership for an Advanced Computing Environment (PACE) computing cluster. A custom dynamic programming algorithm dramatically reduced the computational effort required to generate the solution set. Despite running on a single relatively lower-performance Intel Xeon Gold 6226 processor with 8GB of RAM each, and despite having the computational overhead of automatically initializing, post-processing, and saving solutions, each simulation was completed in average of 2 minutes. This enabled the successful computation of all 86,400 model solves in approximately 1 day of wall-clock time. Automated processing of results and measurement of line dimensions reduced the required storage for solution information to just 10.7 Mb. Thus, this demonstrates the powerful parallelization abilities of the model, which is critical to conducting massive simulation experiments such as this.

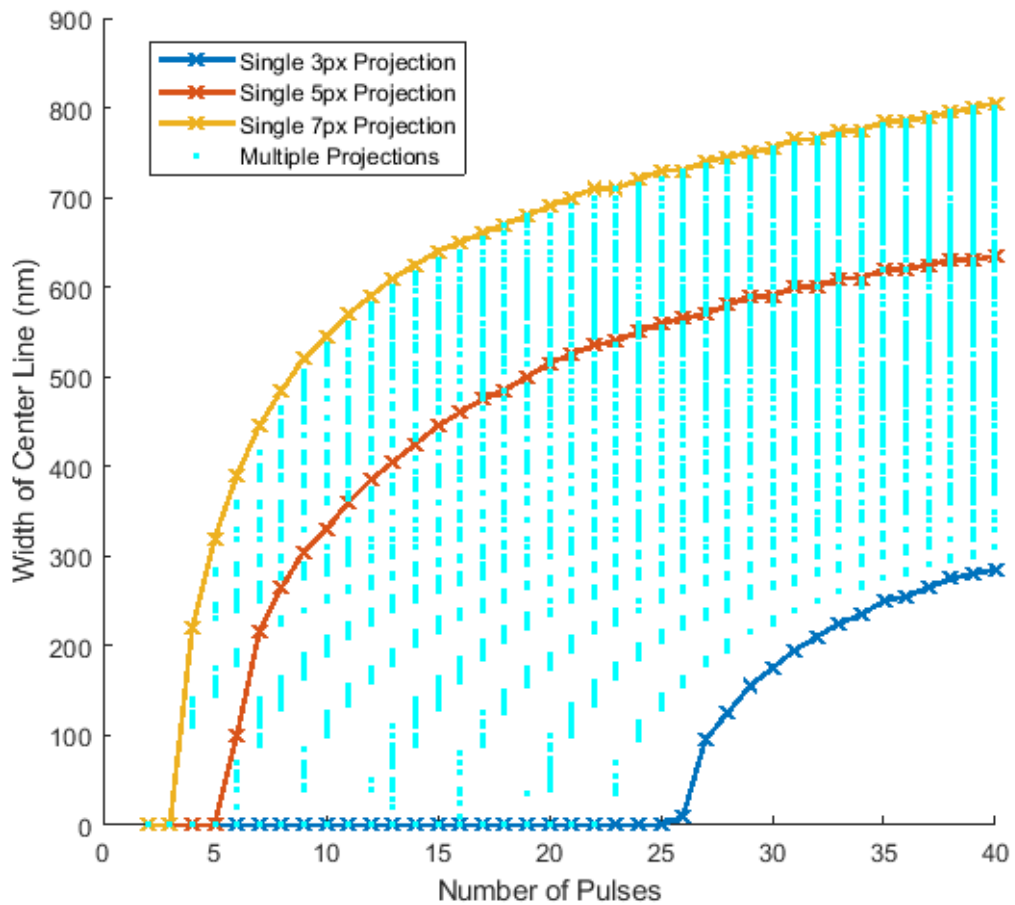


Figure 23: Center line resolutions achievable by multiple projections vs. single projections

Figure 23 shows the widths of all 86,400 center lines. Line plots are used to show the resolution obtainable through single projections of 3px, 5px, and 7px lines. As expected, there is a significant threshold effect that limits the achievable resolution, with very limited access to sub-100nm feature sizes. Combining multiple projections, plotted as blue dots, vastly increases the design space accessible. It is apparent that the results demonstrate that combinations of multiple projections can be used to drive down the

resolution limit. The results demonstrate the possibility of printing all the way down to single-digit nanometers; however, the actual resolution limit is likely governed by the capabilities of the experimental setup to successfully print and develop prints of that size. Nonetheless, the simulation results demonstrate that the physics of P-TPL are not a constraint on resolution when multiple projections are used.

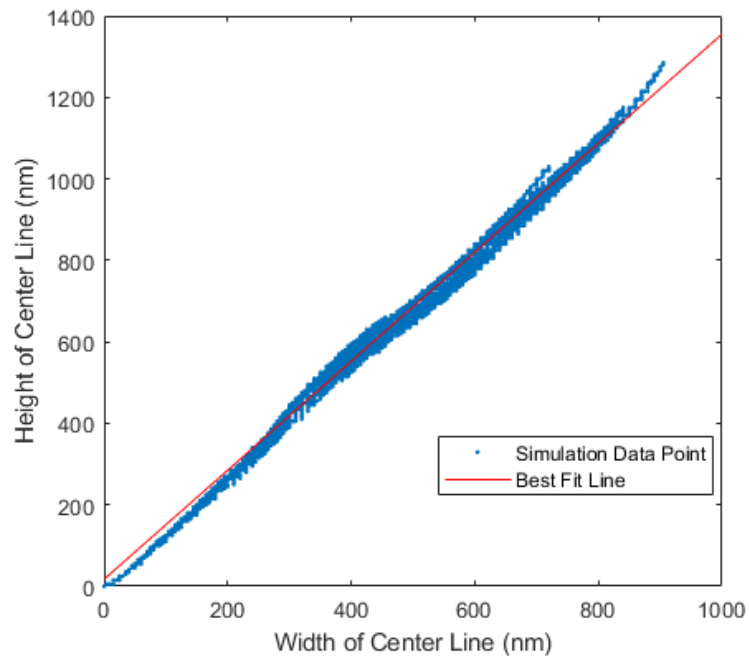


Figure 24: Distribution of center line dimensions

The smallest central line was $5 \text{ nm} \pm 10 \text{ nm}$ in both height and width, and was predicted to be printed after 2 pulses of 3px, followed by a 10ms gap, followed by 24 pulses of 3px. Figure 24 shows that multiple projections allow for the printing of lines with the same width but different heights. The average aspect ratio of the center lines as measured by the best-fit line in Figure 24 is 1.34. However, lines with aspect ratios above and below

this are visible at most widths, showing that combining projections can be used to change the line height without changing the width of the printed lines.

Similarly, it is possible to print different lines with the same width but different DOC. This finding has implications for printing in a way that improves structural and mechanical properties, which often depend on DOC, without compromising resolution.

Figure 25 shows the printable space on a DOC-line width plot.

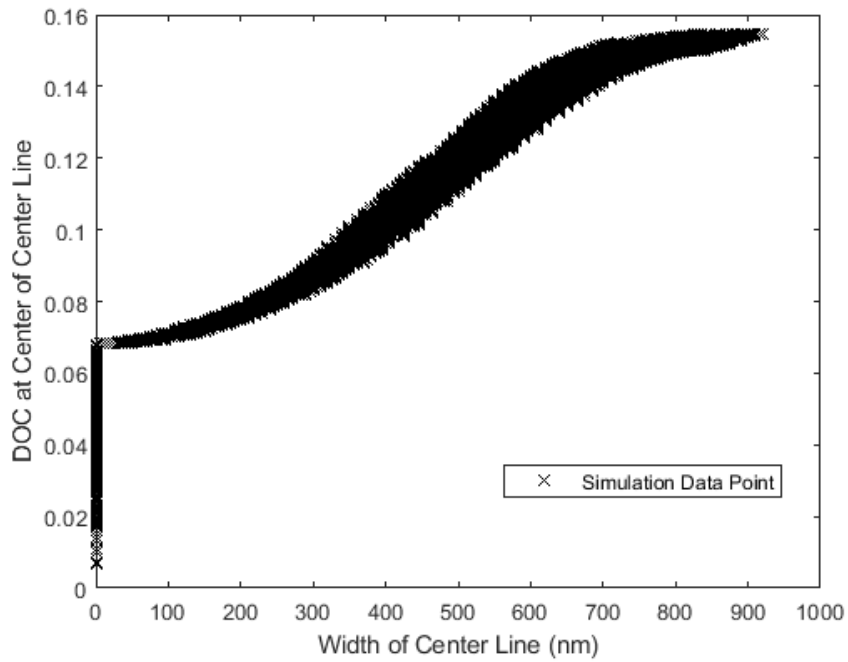


Figure 25: Center line DOC vs. width

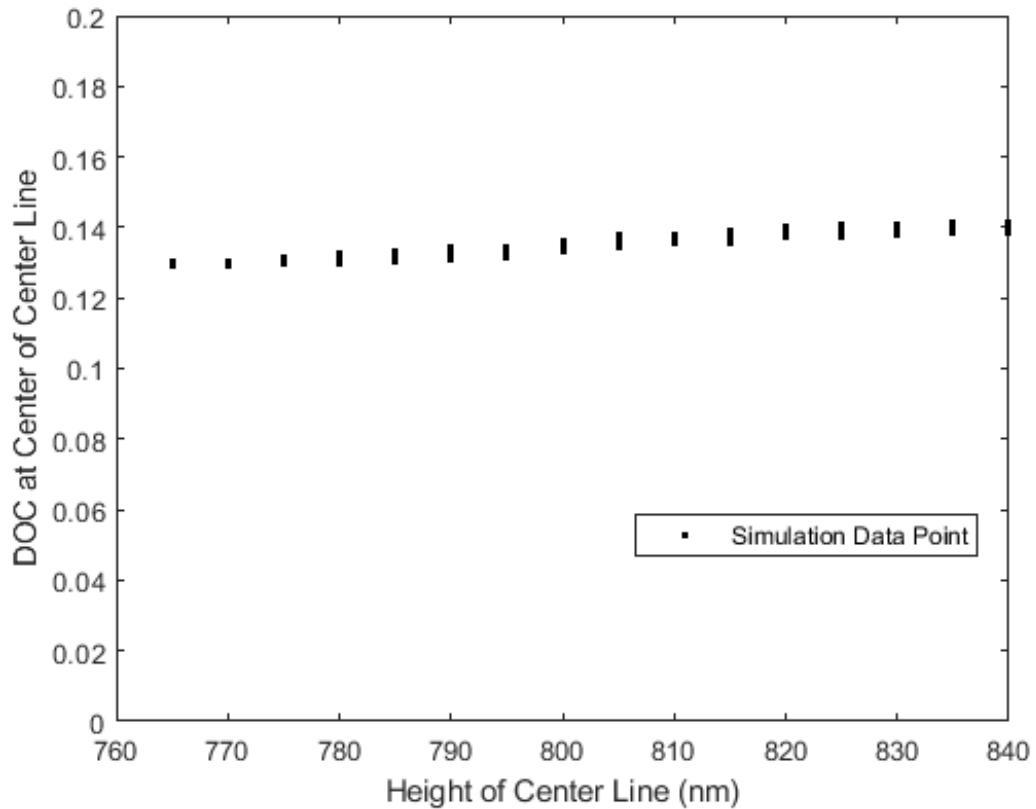


Figure 26: Center line DOC vs. height, constant 600nm width

To see if it is possible to print lines with the same width *and* height but different DOC, Figure 26 shows a plot of only 600 nm wide lines, where there is a relatively wide range of obtainable heights and DOCs. It is seen that it is indeed possible to have lines with the same width and height but of slightly different DOC. However, this parameter space is much smaller than that of Figure 25, indicating that there is a trade-off between controlling aspect ratio and DOC. That is, two degrees of freedom from width, height, and DOC are available under this projection scheme. The discrete x -values seen in Figure 26 is due to the measurement precision of line widths and heights, which were taken to the nearest 10nm for all measurements. Error bars are not plotted due to the large number of datapoints.

Next, the relative sizes of the lines in each projection were studied. The center lines were found to be consistently larger than the others, with the effect most pronounced near the printing threshold, as shown in Figure 27. In some cases, the center lines were the only ones that crossed the threshold and printed. This effect presents another tool with which to control and improve the print resolution.

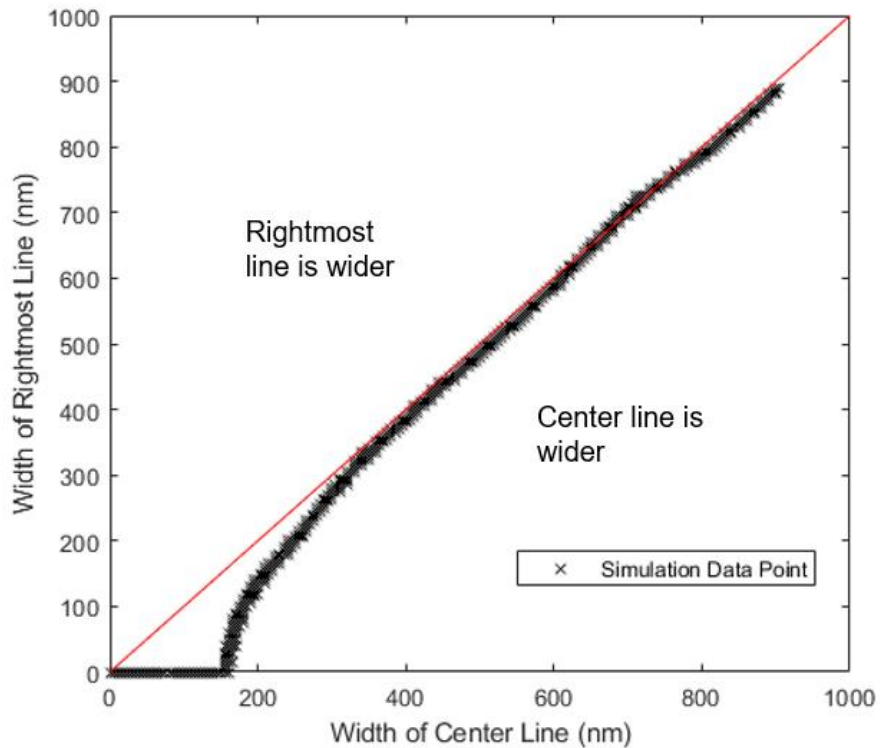


Figure 27: Width of rightmost and center lines

Finally, an investigation of rate-resolution tradeoff was performed. Figure 28 shows the largest and smallest center lines that can be printed in a certain exposure time, where exposure time includes the total time for both pulses and the gap between them, but not the final 100 ms dark period. The maximum width that can be printed was found to increase

with longer exposures as was expected. No strong relationship between the exposure and the minimum width printable was found. Note that due to the nature of the simulation setup, the exposure combinations are strictly defined, so a total exposure time of 4 ms cannot simply be the solution for 2 ms followed by a 2 ms dark period. For this reason, the minimum exposures appear noisier. This finding supports the idea that there is no rate-resolution tradeoff in P-TPL.

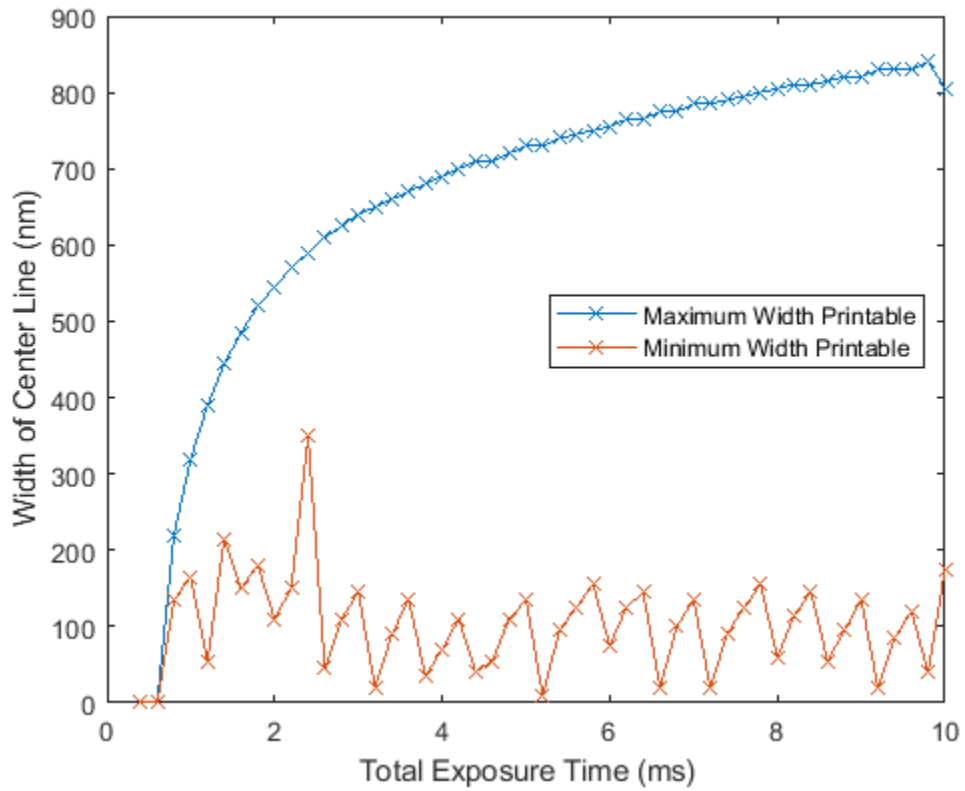


Figure 28: Line width vs. total exposure time

4.3 Generation of Printability Maps

The final study performed was to determine printable parameter regimes using the neural network surrogate model trained in Chapter 3.

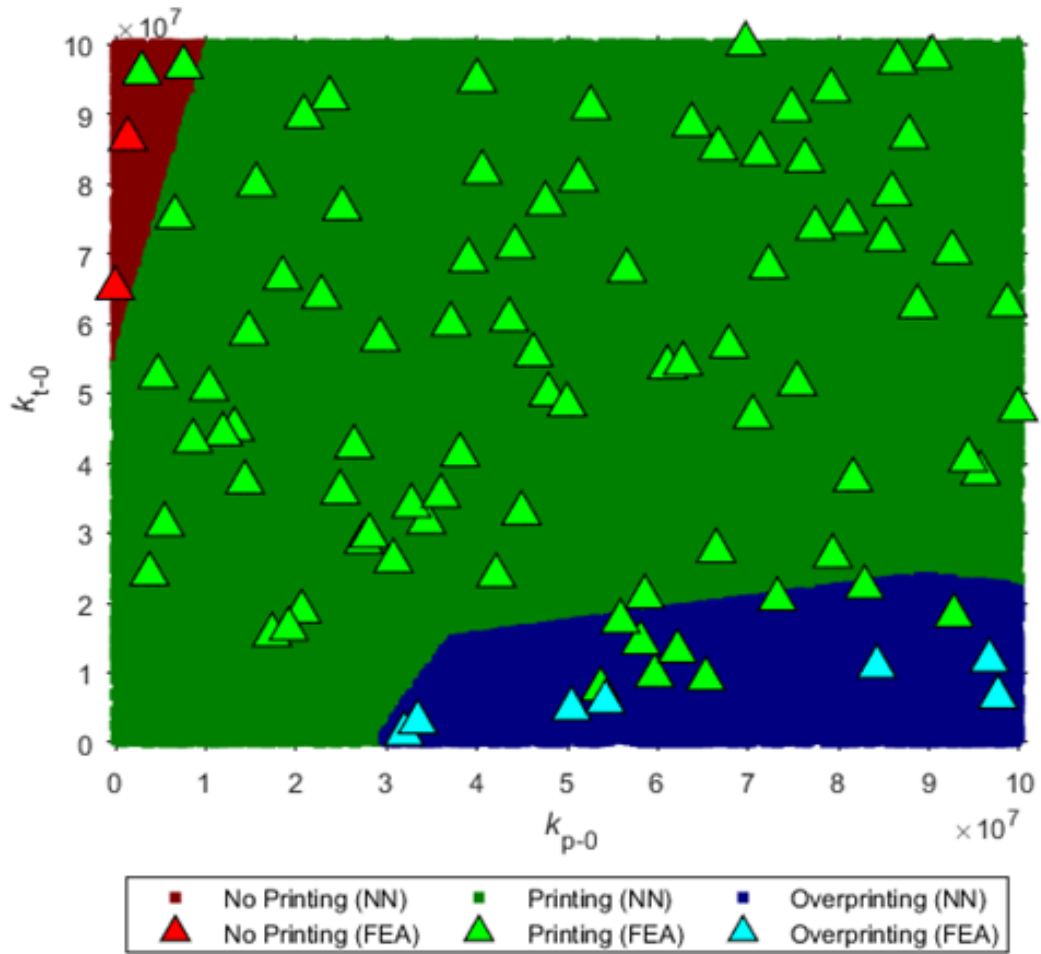


Figure 29: Printability Map, NN & FE datapoints, k_p ($\text{dm}^3/\text{mol}/\text{s}$) - k_t ($\text{dm}^3/\text{mol}/\text{s}$) [43]

Figure 29 shows a printability map of k_p vs. k_t , with other simulation parameters held constant at randomly chosen values. A DOC threshold of 0.20 was used. The

background colors represent results generated by evaluating the NN at densely sampled points. The triangles represent FE results generated at random points for comparison. The NN is seen to correctly predict the approximate limits of printability, although some inaccuracies exist.

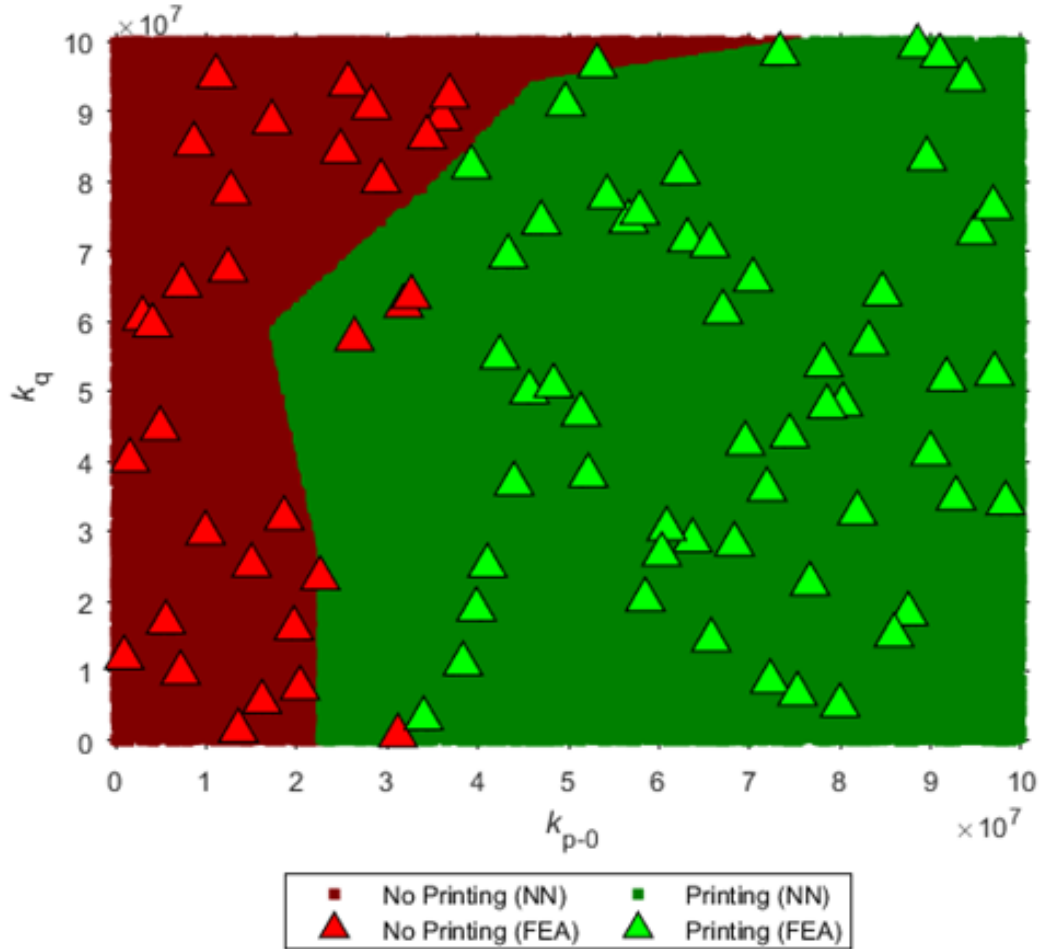


Figure 30: Printability Map, NN & FE datapoints, k_p ($\text{dm}^3/\text{mol/s}$) – k_q ($\text{dm}^3/\text{mol/s}$) [43]

Figure 30 shows similar results for a printability map of k_p vs. k_q with other simulation parameters held constant at another randomly-chosen set of values. Once again, the NN gets the qualitative behavior of the system right, and is able to approximately locate printability limits. Table 4 shows the solve times to generate these two printability maps. Doing even a coarse sampling using FEA takes over an hour, while the neural network can generate thousands of datapoints almost instantaneously. Furthermore, the solve time for FEA is sensitive to the parameter combination being simulated, taking much longer for the more challenging regime in Figure 30. The NN solve time is invariant to the parameter combination being simulated.

Table 4: Comparison of NN and FEA solve times

	Number of datapoints	Time taken to generate
Figure 29: NN	100,000	<1s
Figure 29: FEA	96	7h14min
Figure 30: NN	100,000	<1s
Figure 30: FEA	96	1h19min

CHAPTER 5. CONCLUSION

In this work, the first computational models of the P-TPL nanoscale additive manufacturing process were developed and successfully used to evaluate process limits.

A reaction-diffusion model was built using COMSOL finite element analysis software to solve the mathematical model of P-TPL polymerization. The challenging length and time scales of the process were handled by selective mesh refinement and solver time-stepping respectively. A method of using the polymer solubility threshold to predict feature sizes was developed. The model was successfully calibrated to empirical nanowire width data. Both 2D and 3D simulations were demonstrated.

High performance computing was used to generate a large dataset of FE simulation results conducted across a vast parameter space. A neural network surrogate model was trained on these data and was found to be accurate at classifying parameter combinations as printable or not. The ability to rapidly characterize printability across parameter spaces and generate printability maps using the neural network was demonstrated.

Using the FE model, chemical proximity effects in P-TPL printing were investigated. Diffusion was found to be a relatively weak effect at the chosen printing conditions, being only active at short ranges. Minimizing proximity effects by printing in oxygen-rich conditions was demonstrated. Thus, the ability of P-TPL to print fine porous structures was validated.

Varying the number of pulses in a single exposure was found to give only coarse control of nanowire size, which limited the ability of P-TPL to print sub-100 nm lines.

However, using combinations of multiple exposures with a variable gap between them was shown to give significantly increased control over printing, allowing for the possibility of precisely tuning nanowire width and height, and to a lesser extent degree of conversion. The resolution limits of P-TPL were therefore overcome through combinations of multiple exposures, leading to predicted feature sizes below 50 nm.

Thus, the work in this thesis represents a significant step forward for the development of robust computational tools for two-photon lithography. These simulation capabilities are demonstrably capable of unlocking new insights into process physics and control, and it is hoped that they will substantially accelerate the development and maturing of TPL.

APPENDIX A. HIGH PERFORMANCE COMPUTING TOOLS

High Performance Computing (HPC) is an invaluable tool for scientific discovery through simulation in general, and its use was critical in characterizing P-TPL process limits across a vast parameter space. HPC was performed on the Phoenix computing cluster, part of the Partnership for an Advanced Computing Environment (PACE) at Georgia Tech. This appendix describes the custom computational scripts developed for this purpose.

While the best way to apply HPC varies from problem to problem, a common principle for these simulations is that the fastest way to solve a large number of problems is by assigning no more than one processor to each simulation, as opposed to solving fewer simulations in parallel but assigning multiple cores to each solve. This is a consequence of Amdahl's Law [45], which gives the theoretical limit for the speedup attainable by devoting multiple processors to a workload that is partly parallelizable and has some fraction f that cannot be parallelized [46].

If we consider a P-TPL simulation problem that involves solving on the order of several thousands of simulations using tens to hundreds of processors, Amdahl's Law limits the speedup attainable by assigning $k > 1$ processors to solve a single simulation to $\frac{1}{f + (1-f)/k}$. Thus, even if there was no serial part to a P-TPL simulation, the speedup obtained would only be k , so the time taken to solve all the simulations would be the same as if each simulation was solved independently on a single processor (i.e. $k = 1$), with the number of simulations running being equal to the number of processors available. Exceptions to this

rule (superlinear speedup) can occur in special cases, but none of those apply to P-TPL simulations [47].

In reality, P-TPL simulations, being time-dependent FE simulations, have a significant serial fraction that cannot benefit from having multiple processors available. Thus, the speedup in assigning $k > 1$ processors to solve a single simulation is generally much less than k . The best way to solve a large number of P-TPL simulations that can run independently is to assign one simulation to one processor, repeating until all simulations are completed. This is an “embarrassingly parallel” workload that does not require any communication between parallel jobs, allowing for full exploitation of parallelization. Thus, all parallel P-TPL scripts aimed to run as many jobs in parallel as possible with the given resources.

A.1 Batch Processing on HPC

Collection of data across a multidimensional parameter space presents unique challenges for the use of HPC. Simply submitting thousands of jobs to run on a computing cluster is inefficient due to the overhead in setting up and starting each simulation. In particular, the need to execute a MATLAB script to create an optical dosage interpolation file is a significant draw on resources if repeated every time. In order to optimize this process, a workflow was developed that involved solving batches of simulations with the same dosage distribution and exposure together by taking advantage of COMSOL’s Batch Sweep feature. This workflow is detailed in Figure 31 and was used to generate the training and testing dataset for the surrogate model discussed above.

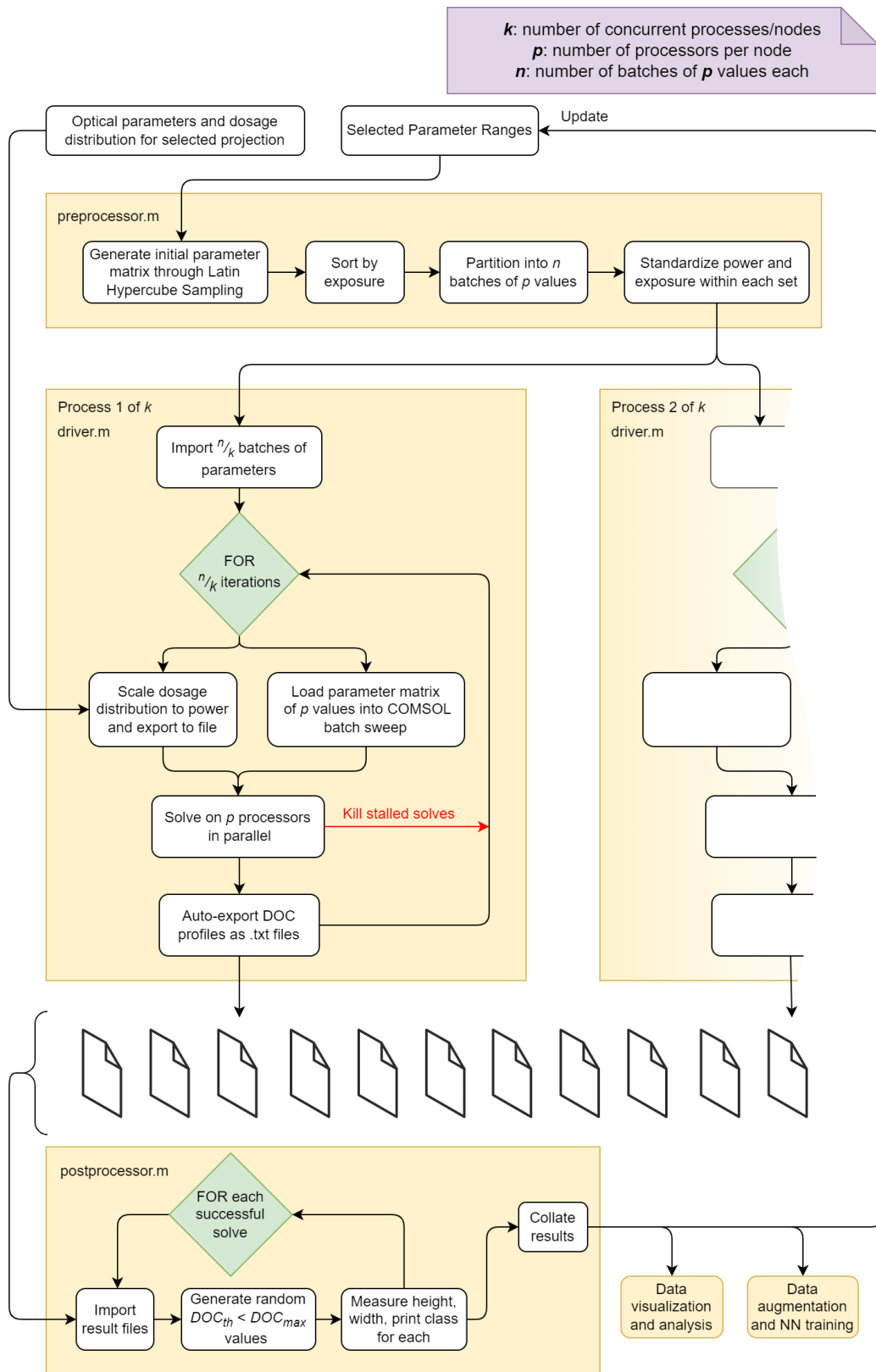


Figure 31: Batch Solving and Processing of FE P-TPL Simulations

The use of MATLAB LiveLink for COMSOL Multiphysics enables a MATLAB script to control COMSOL, allowing for the automation required here. Figure 31 shows that the workflow is split among three MATLAB scripts: a preprocessing and postprocessing script that run serially and a driver for the COMSOL simulations that runs in parallel. Parallelism is not required for preprocessing and postprocessing as these run rapidly even in serial. Although the parameter matrix is generated in the preprocessor through Latin Hypercube Sampling, values of power and exposure are standardized within each batch, accepting coarser sampling for faster solve times. Keeping the exposures the same for each batch makes it less likely that processors are kept idle waiting for other processors to finish solving. In order to optimize even further, the projection is kept the same across all solves, allowing for the optical model to be run once and then scaled according to the optical power for each batch.

COMSOL's Batch Sweep node allows the driver to easily start p parallel solves that then run independently. For the compute nodes on PACE used for data collection, $p = 24$ cores per node, controlled by the single driver script and having 192 GB of shared memory. Several nodes were employed at once, such that $1 \leq k \leq 10$. The solver sequence was modified to include stop conditions to kill stalled solves. This is essential for studies of large parameter spaces, since certain parameter combinations may be significantly more challenging to evaluate (due to exceptionally rapid or slow reactions) than others at the same solver tolerance and mesh refinement. The solver sequence also included an auto-export feature to save DOC profiles along horizontal and vertical axes as text files, thus avoiding the need to save thousands of model result files with larger storage requirements. A single postprocessor read all the saved text files and applied multiple DOC thresholds to

extract several datapoints from each model solve. For NN training, the dataset could be augmented further by generating synthetic datapoints as described in Chapter 3.1.

A.2 Dynamic Programming for Multiple Exposure Studies

While the batch sweep approach was optimal for sweeps over large parameter spaces, the multiple exposure study described in Chapter 4 presented opportunities for further optimization. Generally, the time complexity of a time-dependent FE P-TPL simulation is $O(\text{number of pulses})$. This is because the solver is slowed down near the laser pulses and spends relatively longer computing these time periods than the inter-pulse gaps or the final dark period, as shown in Figure 8. In the multiple exposure study, large pulse counts of up to 40 were used. However, since other parameters were held constant, computations for preceding pulses were essentially repeated. For example, a simulation of 30 pulses and a simulation of 31 pulses proceed identically for the first 30 pulses.

This characteristic can be exploited by implementing a simple dynamic programming scheme. When a problem has overlapping subproblems that a naive algorithm would repeatedly compute, it is possible to implement an approach called memoization to eliminate repeated computations by saving partial solutions. One typical memoization approach involves storing partial solutions as they are generated, and then checking if a solution already exists before generating new ones [48]. Implementing this through a recursion scheme is a common dynamic programming approach and has the benefit of being easy to code, but was found to be unsuitable for P-TPL simulations since the compute nodes did not have enough memory to keep many simulations open at the

same time in the recursive stack. Instead, a “bottom up” iterative approach was implemented. Solutions were saved after each pulse and progressively built up, ensuring that no computations were repeated.

The complete simulation workflow is shown in Figure 32. The value of k for the parameters in Table 3 is 120 (combinations of 3 first line widths and 40 first line exposures). Thus, 120 processors were employed in parallel to solve the 86,400 combinations in approximately 24 hours of wall-time. This dataset is an order of magnitude larger than that collected in Appendix A, demonstrating the performance gains from the dynamic programming approach.

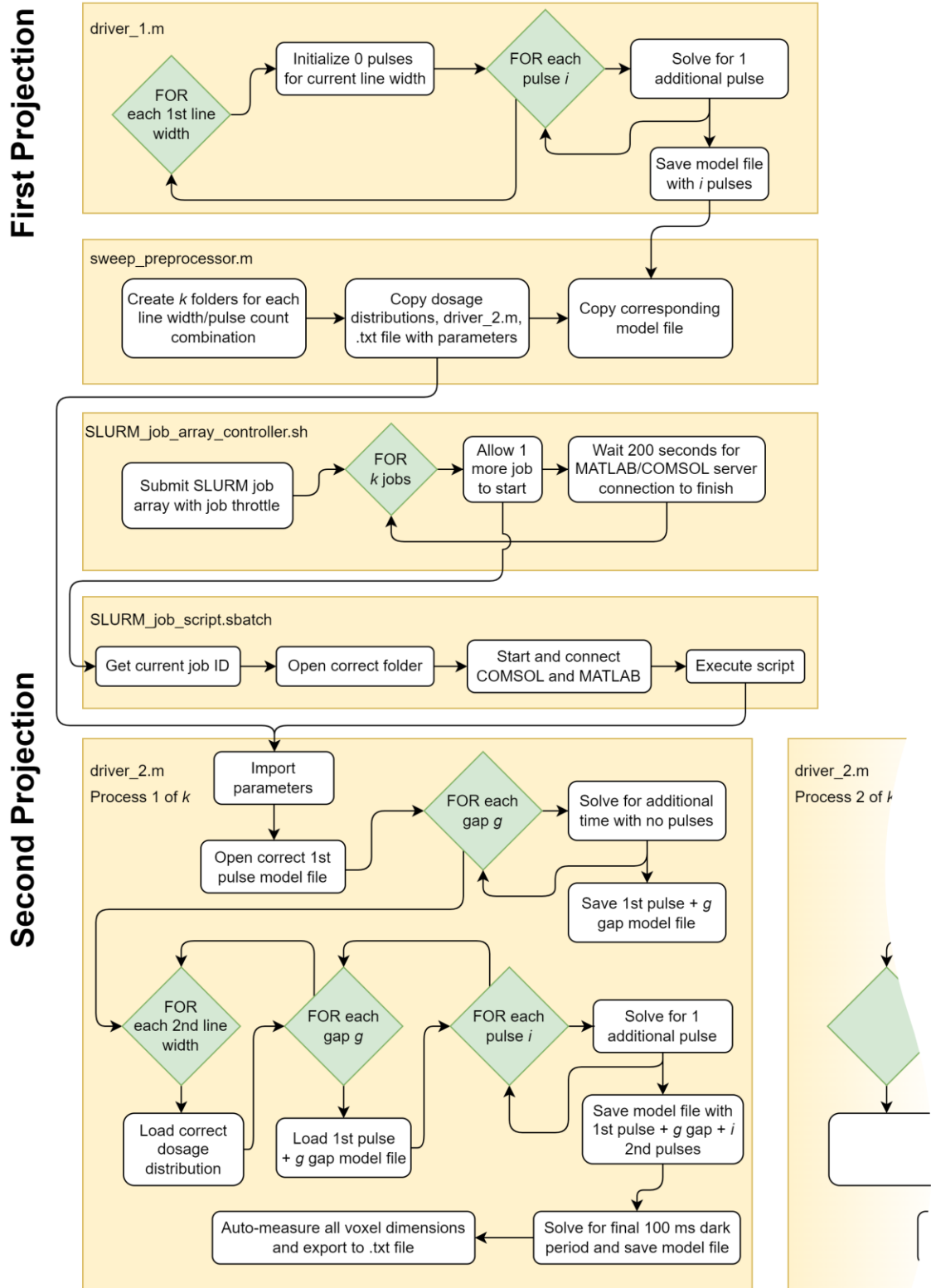


Figure 32: Dynamic Programming Workflow for Multiple Projection Sweep

REFERENCES

1. Harinarayana, V. and Y.C. Shin, *Two-photon lithography for three-dimensional fabrication in micro/nanoscale regime: A comprehensive review*. Optics & laser technology, 2021. **142**: p. 107180.
2. Zheng, L., et al., *Nanofabrication of High-Resolution Periodic Structures with a Gap Size Below 100 nm by Two-Photon Polymerization*. Nanoscale Research Letters, 2019. **14**(1).
3. Malinauskas, M., et al., *Ultrafast laser nanostructuring of photopolymers: A decade of advances*. Physics Reports, 2013. **533**(1): p. 1-31.
4. Dyck, O., A.R. Lupini, and S. Jesse, *Atom-by-Atom Direct Writing*. Nano Letters, 2023. **23**(6): p. 2339-2346.
5. Kaiser, W. and C.G.B. Garrett, *Two-Photon Excitation in $\text{CaF}_2:E^{2+}$* . Physical Review Letters, 1961. **7**(6): p. 229-231.
6. Li, L. and J.T. Fourkas, *Multiphoton polymerization*. Materials today., 2007. **10**(6): p. 30-37.
7. Cumpston, B.H., et al., *Two-photon polymerization initiators for three-dimensional optical data storage and microfabrication*. Nature, 1999. **398**(6722): p. 51-54.
8. Monroe, B.M. and G.C. Weed, *Photoinitiators for free-radical-initiated photoimaging systems*. Chemical Reviews, 1993. **93**(1): p. 435-448.
9. Andrzejewska, E., *Free Radical Photopolymerization of Multifunctional Monomers*. Three-Dimensional Microfabrication Using Two-photon Polymerization, 2016: p. 62-81.
10. Golvari, P. and S.M. Kuebler, *Fabrication of Functional Microdevices in SU-8 by Multi-Photon Lithography*. Micromachines, 2021. **12**(5): p. 472.
11. Faraji Rad, Z., P.D. Prewett, and G.J. Davies, *High-resolution two-photon polymerization: the most versatile technique for the fabrication of microneedle arrays*. Microsystems & Nanoengineering, 2021. **7**(1).
12. Li, J., et al., *Ultrathin monolithic 3D printed optical coherence tomography endoscopy for preclinical and clinical use*. Light: Science & Applications, 2020. **9**(1).

13. Schmid, M., et al., *3D printed hybrid refractive/diffractive achromat and apochromat for the visible wavelength range*. Optics Letters, 2021. **46**(10): p. 2485.
14. Dietrich, P.-I., et al., *In situ 3D nanoprinting of free-form coupling elements for hybrid photonic integration*. Nature Photonics, 2018. **12**(4): p. 241-247.
15. Lay, C.L., et al., *Two-Photon-Assisted Polymerization and Reduction: Emerging Formulations and Applications*. ACS Applied Materials & Interfaces, 2020. **12**(9): p. 10061-10079.
16. Oakdale, J.S., et al., *Direct Laser Writing of Low-Density Interdigitated Foams for Plasma Drive Shaping*. Advanced Functional Materials, 2017. **27**(43): p. 1702425.
17. Selimis, A., V. Mironov, and M. Farsari, *Direct laser writing: Principles and materials for scaffold 3D printing*. Microelectronic Engineering, 2015. **132**: p. 83-89.
18. Schade, R., et al., *Two-Photon Techniques in Tissue Engineering*. The International Journal of Artificial Organs, 2010. **33**(4): p. 219-227.
19. Xiong, W., et al., *Laser-Directed Assembly of Aligned Carbon Nanotubes in Three Dimensions for Multifunctional Device Fabrication*. Advanced Materials, 2016. **28**(10): p. 2002-2009.
20. Sima, F., et al., *Three-dimensional femtosecond laser processing for lab-on-a-chip applications*. Nanophotonics, 2018. **7**(3): p. 613-634.
21. Wu, S., J. Serbin, and M. Gu, *Two-photon polymerisation for three-dimensional micro-fabrication*. Journal of Photochemistry and Photobiology A: Chemistry, 2006. **181**(1): p. 1-11.
22. Huang, T.-Y., et al., *3D Printed Microtransporters: Compound Micromachines for Spatiotemporally Controlled Delivery of Therapeutic Agents*. Advanced Materials, 2015. **27**(42): p. 6644-6650.
23. Tian, Y., et al., *Fabrication and Characterization of Photonic Crystals in Photopolymer SZ2080 by Two-Photon Polymerization Using a Femtosecond Laser*. Journal of Micro and Nano-Manufacturing, 2014. **2**(3).
24. Gissibl, T., et al., *Two-photon direct laser writing of ultracompact multi-lens objectives*. Nature Photonics, 2016. **10**(8): p. 554-560.
25. Meza, L.R., S. Das, and J.R. Greer, *Strong, lightweight, and recoverable three-dimensional ceramic nanolattices*. Science, 2014. **345**(6202): p. 1322-1326.
26. Amato, L., et al., *Integrated three-dimensional filter separates nanoscale from microscale elements in a microfluidic chip*. Lab on a Chip, 2012. **12**(6): p. 1135-1142.

27. Portela, C.M., et al., *Supersonic impact resilience of nanoarchitected carbon*. Nature Materials, 2021. **20**(11): p. 1491-1497.
28. Niesler, F. and M. Hermatschweiler, *Two-Photon Polymerization - A Versatile Microfabrication Tool*. Laser Technik Journal, 2015. **12**(3): p. 44-47.
29. Bunea, A.-I., et al., *Micro 3D Printing by Two-Photon Polymerization: Configurations and Parameters for the Nanoscribe System*. Micro, 2021. **1**(2): p. 164-180.
30. Cao, C., et al., *Click chemistry assisted organic-inorganic hybrid photoresist for ultra-fast two-photon lithography*. Additive manufacturing., 2022. **51**: p. 102658.
31. Saha, S.K., et al., *Scalable submicrometer additive manufacturing*. Science, 2019. **366**(6461): p. 105-109.
32. Oakdale, J.S., et al., *Post-print UV curing method for improving the mechanical properties of prototypes derived from two-photon lithography*. Optics Express, 2016. **24**(24): p. 27077.
33. Hadibrata, W., et al., *Inverse Design and 3D Printing of a Metalens on an Optical Fiber Tip for Direct Laser Lithography*. Nano Letters, 2021. **21**(6): p. 2422-2428.
34. Uppal, N. and P. Shiakolas, *Modeling of temperature-dependent diffusion and polymerization kinetics and their effects on two-photon polymerization dynamics*. Journal of Micro/Nanolithography, MEMS, and MOEMS, 2008. **7**(4): p. 043002.
35. Mueller, J.B., et al., *Polymerization Kinetics in Three-Dimensional Direct Laser Writing*. Advanced Materials, 2014. **26**(38): p. 6566-6571.
36. Pingali, R. and S.K. Saha, *Reaction-Diffusion Modeling of Photopolymerization During Femtosecond Projection Two-Photon Lithography*. Journal of manufacturing science and engineering., 2022. **144**(2): p. 1.
37. Jariwala, A.S., et al., *Modeling effects of oxygen inhibition in mask-based stereolithography*. Rapid Prototyping Journal, 2011. **17**(3): p. 168-175.
38. Rumi, M., et al., *Structure–Property Relationships for Two-Photon Absorbing Chromophores: Bis-Donor Diphenylpolyene and Bis(styryl)benzene Derivatives*. Journal of the American Chemical Society, 2000. **122**(39): p. 9500-9510.
39. Sigma-Aldrich. *Pentaerythritol Triacrylate*. Available from: <https://www.sigmaaldrich.com/catalog/product/aldrich/246794?lang=en®ion=US>.
40. Lagarias, J.C., et al., *Convergence Properties of the Nelder--Mead Simplex Method in Low Dimensions*. SIAM Journal on Optimization, 1998. **9**(1): p. 112-147.

41. McBride, K. and K. Sundmacher, *Overview of Surrogate Modeling in Chemical Process Engineering*. Chemie Ingenieur Technik, 2019. **91**(3): p. 228-239.
42. Zou, J., Y. Han, and S.-S. So, *Overview of Artificial Neural Networks*, in *Methods in Molecular Biology*TM. 2008, Humana Press. p. 14-22.
43. Pingali, R. and S. Saha, *Printability Prediction in Projection Two-Photon Lithography via Machine Learning Based Surrogate Modeling of Photopolymerization*, in *Manufacturing Science and Engineering Conference 2023*. 2023, ASME: New Brunswick, New Jersey.
44. McKay, M.D., R.J. Beckman, and W.J. Conover, *A Comparison of Three Methods for Selecting Values of Input Variables in the Analysis of Output from a Computer Code*. Technometrics, 1979. **21**(2): p. 239-245.
45. Amdahl, G.M., *Validity of the Single Processor Approach to Achieving Large Scale Computing Capabilities*, Reprinted from the *AFIPS Conference Proceedings, Vol. 30 (Atlantic City, N.J., Apr. 18–20)*, AFIPS Press, Reston, Va., 1967, pp. 483–485, when Dr. Amdahl was at Inte. IEEE Solid-State Circuits Newsletter, 2007. **12**(3): p. 19-20.
46. Al-Hayanni, M.A.N., et al., *Amdahl's law in the context of heterogeneous many-core systems – a survey*. IET Computers & Digital Techniques, 2020. **14**(4): p. 133-148.
47. Gustafson, J.L., *Amdahl's Law*, in *Encyclopedia of Parallel Computing*, D. Padua, Editor. 2011, Springer US: Boston, MA. p. 53-60.
48. Kumar, P., *Dynamic programming*. The Control Handbook, 2010. **63**: p. 1097-1.